Universidad de Santiago de Compostela
Departamento de Física de Partículas

# Simulación del experimento SOFIA del GSI para estudios de fisión en cinemática inversa.

**José Luis Rodríguez Sánchez**
Santiago de Compostela, Junio 2012

Universidad de Santiago de Compostela
Departamento de Física de Partículas

# Simulation of the SOFIA experiment at GSI for fission studies in inverse kinematics.

**José Luis Rodríguez Sánchez**
Santiago de Compostela, June 2012

# Contents

**Contents** IV

**1 Introduction** 8

**2 The SOFIA Experiment** 12
2.1 Implementation of the SOFIA setup in the simulation . . . . . 13
2.1.1 The liquid hydrogen target . . . . . . . . . . . . . . . . 16
2.1.2 The active target . . . . . . . . . . . . . . . . . . . . . 16
2.1.3 The twin MUSIC . . . . . . . . . . . . . . . . . . . . . 17
2.1.4 The MWPC . . . . . . . . . . . . . . . . . . . . . . . . 18
2.1.5 ToF-walls . . . . . . . . . . . . . . . . . . . . . . . . . 18
2.1.6 The LAND detector . . . . . . . . . . . . . . . . . . . 19
2.1.7 ALADIN dipole . . . . . . . . . . . . . . . . . . . . . . 20

**3 Description of the simulation** 24
3.1 Reaction codes: INCL+ABLA and ABRABLA . . . . . . . . . . 24
3.2 The AMADEUS code . . . . . . . . . . . . . . . . . . . . . . . 27
3.3 The Geant4 code . . . . . . . . . . . . . . . . . . . . . . . . . 27
3.3.1 Introduction . . . . . . . . . . . . . . . . . . . . . . . . 27
3.3.2 Energy loss . . . . . . . . . . . . . . . . . . . . . . . . 27
3.3.3 Energy straggling . . . . . . . . . . . . . . . . . . . . . 33
3.3.4 Angular straggling . . . . . . . . . . . . . . . . . . . . 36

**4 Results of the simulation** 40
4.1 Detection efficiency . . . . . . . . . . . . . . . . . . . . . . . . 40
4.1.1 Simulation of the reaction conditions . . . . . . . . . . 40
4.1.2 Detection efficiency of fission fragments . . . . . . . . . 41
4.1.3 Detection efficiency of light-charged particles . . . . . . 44
4.1.4 Detection efficiency of neutrons . . . . . . . . . . . . . 47
4.2 Reconstruction of the mass number . . . . . . . . . . . . . . . 50
4.2.1 Results of the reconstruction . . . . . . . . . . . . . . . 52

**Conclusions** 60

**Bibliography** 70

**List of Figures** 72

# Chapter 1

# Introduction

Nuclear Physics is a discipline where new frontiers are open up continuously. Many scientists have made big efforts during the last century in getting a better understanding of the constituents of our Universe bound by the strong interaction: hadrons, atomic nuclei and some stelar systems. One of the most fascinating phenomenon that has attrached the attention of Nuclear Physicist is nuclear fission. Nuclear fission was discovered by O. Hahn and F. Strassmann in 1938 when they studied the Uranium reactions. After the name "fission" was given by L. Meitner and O.R. Frischand and the first model to explain the nuclear fission was proposed by N. Böhr and J. Wheeler [1] in 1939. In 1942 and 1945 the first nuclear pile and the first atomic weapon were built, respectively, in which worked scientists as H. Moseley, R. Oppenheimer, N. Böhr, E. Fermi, R. Feynman, etc. Actually the fission is one of the most widely used nuclear process, e.g., we use it in nuclear powerplants to generate electric power, to produce radio tracers for medical imaging and to produce nuclei for from stability to investigate the isospin dependence of the nuclear force, but a complete understanding of this process has not yet being achieved. Moreover, from an experimental view point, the combined measurement of the mass and charge of both fission fragments remains a challenge more than 70 years after the discovery of this process.

Nuclear fission is also an appropiate tool for studying nuclear structure at large deformation and the link between intrinsic and collective excitation in nuclei. These two processes manifest in two different energy regimes:

- Fission induced at low-excitation energy: In this case we study the nuclear structure at large deformation (shell effects). It is known that the asymmetry in the mass or charge distribution of the fission fragments has at its origin the shell effects. In principle it was thought that shell closures at N=82 and

Z=50 were responsible for the observed asymmetries. However, recent results [2] indicate that the charge distribution of heavy fission fragments peak at Z=54 and not at Z=50 (see figure 1.1 a)). Recently we have also observed a asymmetric mass distribution of the fission fragments of $^{180}$Hg [3], with the most probable light and heavy masses of $A_L$= 80 and $A_H$= 100 (see figure 1.1 b)) which is not expected. These effects can be investigated in coulomb induced fission reactions with relativistic $^{238}$U projectiles.

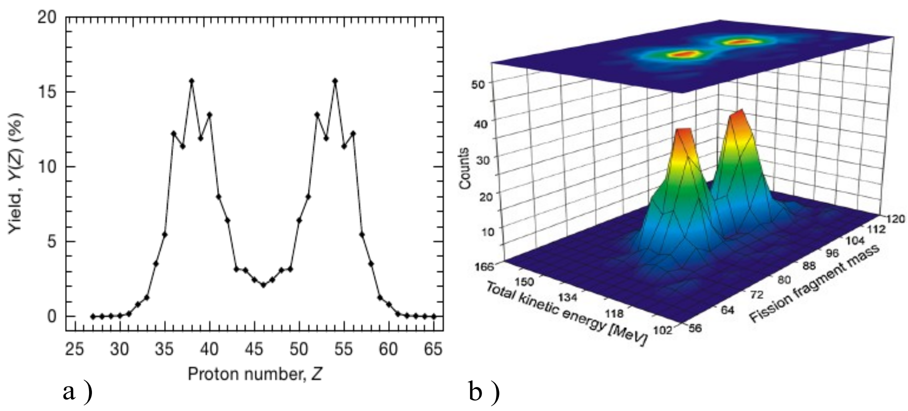


***Figure 1.1:*** *a) We observe shell effects where the fission happens with Z=54 when one expect that it happens with Z=50. b) Asymmetric observed in the fission of $^{180}$Hg where the most probable light and heavy masses are $A_L$= 80 and $A_H$= 100, which is not expected.*

- Fission induced at high-excitation energy: This case allows to study the coupling between intrinsic and collective excitation in nuclei that can be described as a dissipation process characterized by a friction coeficient. Fission probabilities and the final distributions of fission fragments are expected to be sensitive to this friction parameter. We will study this mechanism in $^{208}$Pb+p collision at 500 A MeV.

The new experiment SOFIA aims at investigating both, structural and dynamical effects in fission, measuring for the first time the charge, the mass and the kinetic energy of the two fission fragments. To perform these measurements we will take advantage of the inverse kinematics where fission fragments are produce with large kinetic energies under such conditions the atomic number of the two fragments can be determined from their energy loss in a double ionisation chamber and the mass number from the measurement of their magnetic rigidity and velocity using a large acceptance dipole magnet, tracking detectors and time of flight detectors. The aim of this work is to develop a complete simulation of the SOFIA experiment using event generators describing the fission physics and transport codes to describe the propagation of ions and particles through the experimental setup. This simulation will be used to optimize the geometrical efficiency of the experimental setup but also to investigate the reconstruction of the mass number of the fission fragments and determine the final resolution we can achieve. The work is organised as follows. In chapter 2 we describe the experimen. Chapter 3 details the simulation and its validation. In chapter 4 we present the main results concerning detection efficiency of fission fragments, neutrons and light-charged particles and the reconstruction of the mass number of the fission fragments.

# Chapter 2

# The SOFIA Experiment

SOFIA (**S**tudies **O**n **FI**ssion with **A**ladin) is first step of the forth coming GSI fission experiment program. SOFIA will benefit from relativistic actinide beams avaliable at GSI [4] to induce electromagnetic fission and spallation-fission in inverse kinematics. It will take place in Cave C (see figure 2.1) in the current GSI facility. SOFIA will enable to determine the nuclear charge, the mass and the kinetic energy for each fission fragment as well as the neutron multiplicity and detect light charged particles. In this chapter we present the setup and we explain the different detectors that we will use in the experiment.

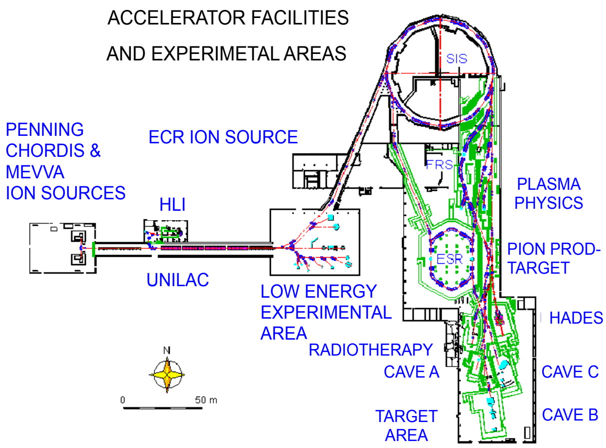


***Figure 2.1:*** *The GSI (Darmstadt) experimental facilities. In this drawing we can observe the two acceleration stages, the UNILAC and SIS, and the experimental areas, in particular the Fragment Separator (FRS) and Cave C.*

## 2.1 Implementation of the SOFIA setup in the simulation

The SOFIA experimental setup was designed to investigate fission in inverse kinematics. The fissile nucleus is accelerated at relativistic energies and the produced fission fragments are emitted forward with large kinetic energies. These conditions will allow to determine the mass and atomic numbers of both fragments. Under such kinematics conditions one can induce low-excitation energy fission via coulomb excitation reactions and hight-excitation energy fission in nuclear collisions. In this experiment we will study the fission of $^{238}$U and $^{208}$Pb. The $^{238}$U fission is produced in an active target (see figure 2.6) and the $^{208}$Pb fission is produced in a $H_2$ target (see figure 2.5). In the case of $^{238}$U, the relativistic energy of the actinide beam (500 A Mev) will lead to a Lorentz contraction of the electromagnetic field of the target in the orthogonal direction of the trajectory. The impulsion felt by the projectile is comparable to a gamma absorption (virtual photon). The energy transferred to the incident proyectile will be sufficient to excite the giant dipole resonance that eventually will decay by fission. Due to the kinematics of the reactions, both fission fragments are focused in the beam direction within a 40 mrad angular cone, as it is shown in the figure 2.2. In the case of $^{208}$Pb, the beam produces spallation-fission on $H_2$

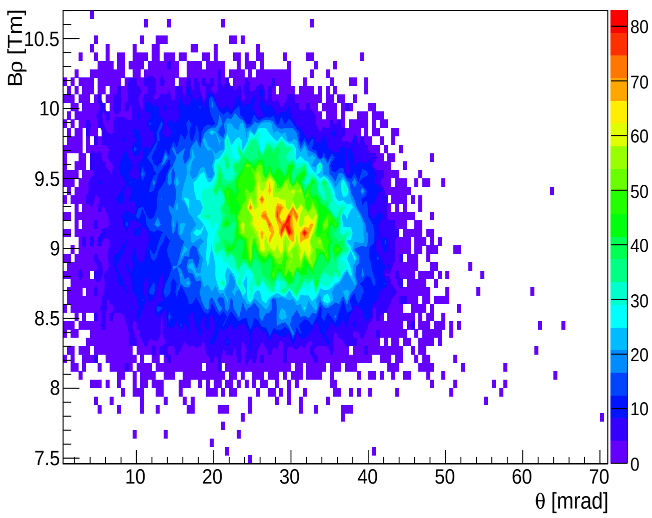


***Figure 2.2:*** *Bρ vs. θ for the fission fragments produced in the fission of $^{238}U$ at 500 A MeV, we have used ABRABLA code to simulate this figure.*

target. The nuclei loses nucleons in the collision and gains excitation energy, then the nucleus de-excitates by particle evaporation or fission. Again both fission fragments are focused in the beam direction within a 40 mrad angular cone, as it is shown in the figure 2.3. Therefore, the experimental setup must cover the forward angles being capable of providing the atomic number of the fission fragments from energy loss and their mass number from magnetic rigity and time-of-flight. The setup that we will use in this experimet is drawn in figure 2.4, it consists in two targets (Active target and $H_2$ target to study $^{238}U+^{238}U$ and $^{208}Pb+p$ collisions, respectively), a double ionisation chamber (Twin MUSIC) which determines the atomic number, two MWPCs to determine the magnetic rigidity, two ToF-walls to measure time-of-flight, a neutron detector (LAND) to measure the neutron multiplicity, a magnet (ALADIN) and different pipes. In principle, to determine the mass of the fission fragments we will need detectors with position resolution of 200 $\mu m$ and time resolution of 40 ps both FWHM.

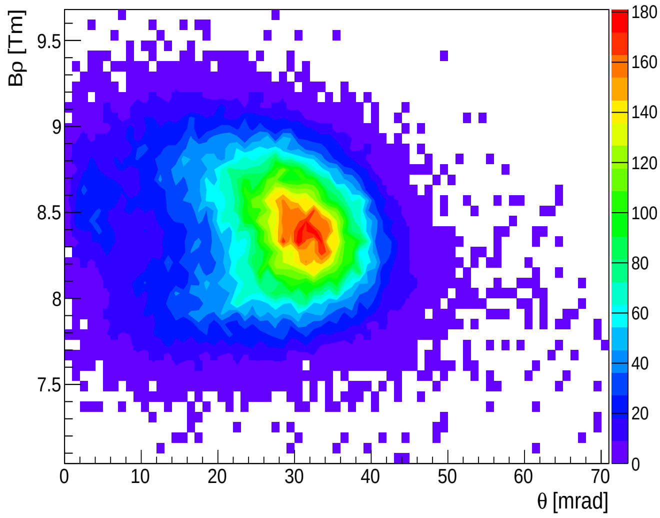


***Figure 2.3:*** *Bρ vs. θ for the fission fragments produced in the fission of* $^{208}Pb$ *at 500 A MeV, we have used INCL+ABLA code to simulate this figure.*

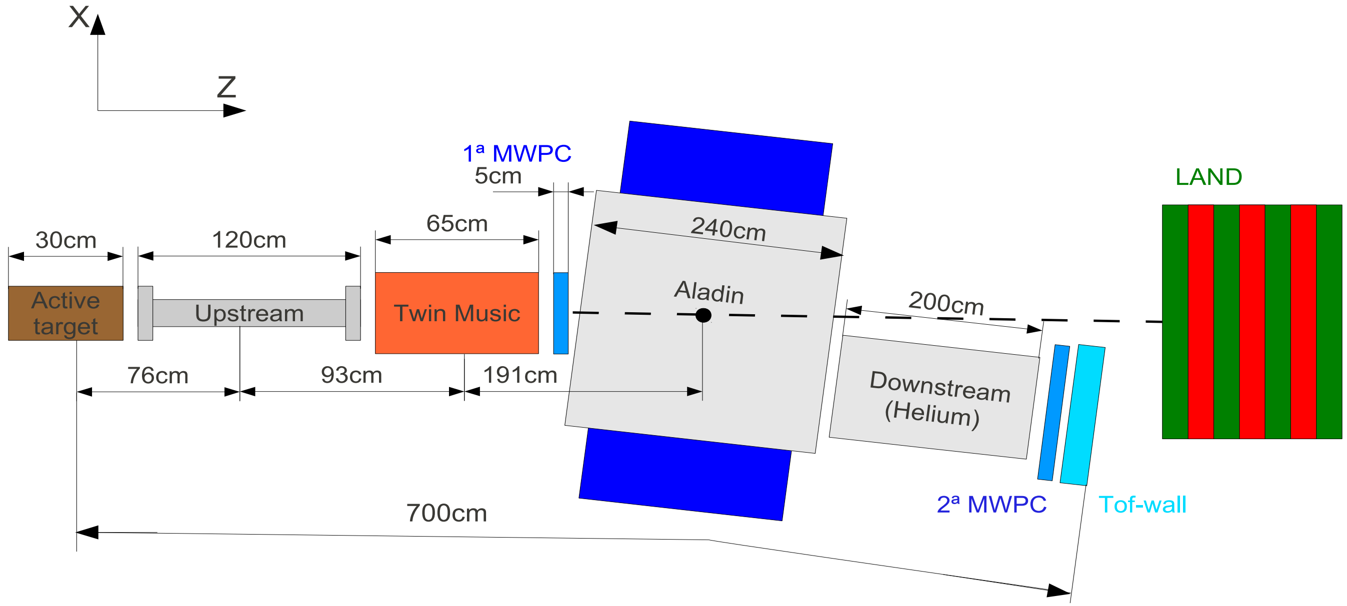


| Active target | Vacuum pipe | Twin Music | MWPC | Aladin | Helium pipe |
|---|---|---|---|---|---|
| Ar 21 cm<br>Mylar 2×6 µm<br>Al 4×50 µm<br>U 2×0.6 mm<br>Pb 0.125 mm | Kapton 2×50 µm<br>Vacuum 120 cm | Mylar 2×7µm<br>Ne (80%) $CH_4$ (20%) 60 cm | Kapton 4×20 µm<br>Ar 3 cm | Kapton 35 µm<br>He 220 cm | Kapton 3×35 µm<br>He 190 cm<br>Air 10 cm |

***Figure 2.4:*** *Experimental setup for the SOFIA experiment, we will use this setup for the* $^{238}U$+$^{238}U$ *collision, in the case* $^{208}Pb$+$p$ *we will change the active target by* $H_2$ *target and we will put a ToF-wall for light charged particles between vacuum pipe and Twin MUSIC.*

### 2.1.1 The liquid hydrogen target

A hydrogen target is needed (figure 2.5) to investigate the nuclear reactions occuring in the interaction of Pb with protons in inverse kinematics. The target was built at the laboratory Saturne in Saclay, France. It is a cylinder with a diameter of 3 cm and a length of 1 cm. The hydrogen is cooled down to about 20 K and stored in a cryogenic titanium vessel at the pressure of 1.036 atm. The vessel is inside another titanium container (30 $\mu$m), and some foils of mylar and aluminium (30 $\mu$m) are inserted between the two in order to ensure thermal insulation. The encapsulation of the vessel has to guarantee, in case of an eventual leakage, a safe interface between the target and beam line. The hydrogen thickness in the centre can be determined with energy loss measurement, and it is of 87.3 $\pm$ 2.2 mg/cm$^2$. The probability for projectile nuclear interactions of amounts to about 10% whereas the secondary interaction probability is of 0.5%.

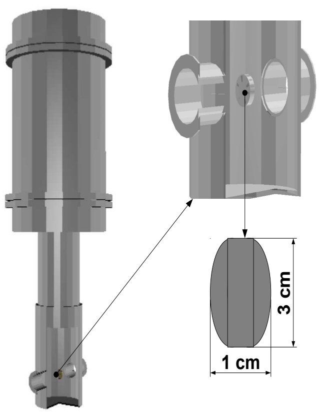


***Figure 2.5:*** *$H_2$ target.*

### 2.1.2 The active target

We have build an active target to invetigate the electromagnetic reactions occuring in the interaction of uranium with lead or uranium. The active target is composed by layers of lead and layers of uranium inside a stainless steel cylinder with a diameter of 26.1 cm and weights 30 kg. The entrance and exit windows are 6 $\mu$m thicknesses the mylar foils. The lead layer is of 0.125 mm thickness and the uranium layers are of 0.6 mm thicknesses (see figure 2.6). The system allows to determine in which layer of the target the reaction takes place.

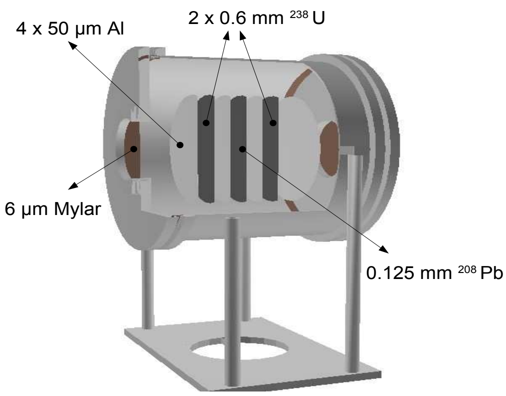


***Figure 2.6:*** *Active target.*

### 2.1.3 The twin MUSIC

The identification in atomic number is done using a double ionisation chamber (**MU**lti-**S**ampling **I**onization **C**hamber with two identical active volumes), located after the active target. The energy loss of both fragments is determined in each part of the chamber. The detector provides low mass in directions longitudinal to the beam in order to minimize secondary reactions and angular straggling.

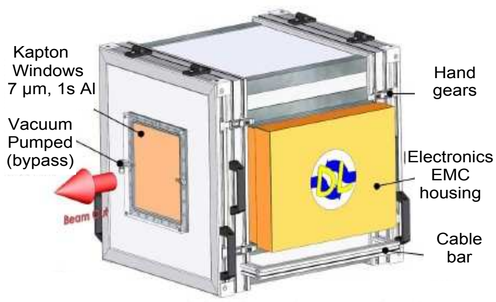


***Figure 2.7:*** *Twin MUSIC.*

The housing is made of standard industrial aluminium profiles and weights 150 kg. It is a faraday cage which may be evacuated slightly down to 500 mbar in order to support and fasten changes of the gas composition. The entrance and exit windows are 7 $\mu$m thicknesses the kapton foils. The chamber (see figure 2.7) is operated with gas mixture based on Neon (80 %) and $CH_4$ (20 %) that provides a fast drift of the charges generated (2 cm/$\mu$s) and a low diffusion. The total active volume is 200×200×500 $mm^3$, it consists of 20 rectangular sectors of 100×200×50 $mm^3$, 10 for each side. The maximun electric field is 500 V/cm, the energy loss resolution is 2% and the horizontal position resolution is 200 $\mu$m (FWHM).

### 2.1.4 The MWPC

MWPC is a **M**ulti-**W**ire **P**roportional **C**hambers. It is made of Aluminium and the windows are 20 $\mu$m thicknesses the kapton foils (see figure 2.8). It has a gas mixture based on Argon and $CH_4$ and provides 200 $\mu$m horizontal position resolution and 2 mm vertical position resolution.

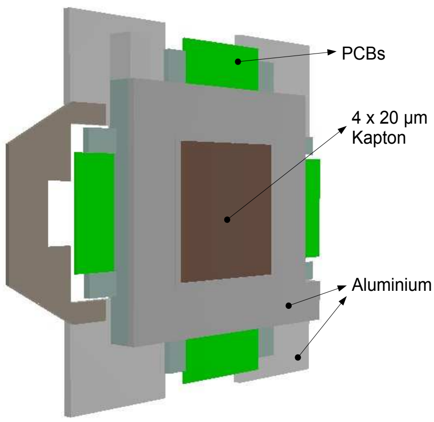


***Figure 2.8:*** *MWPC.*

### 2.1.5 ToF-walls

The detector of the figure 2.9(a) is used to measure light chaged particles, it consists of two crossed layers of 50×50 $cm^2$ each with 8 paddles, the paddles are 48×6×0.5 $cm^3$ and the time resolution is approximately of 250 ps (FWHM). We will put this detector between the vacuum pipe and the Twin MUSIC and we will remove two vertical and two horizontal paddles which will leave a space of 12×12 $cm^2$ for the transmission of the fission fragments. In addition the ToF-wall for fission fragment is shown in the figure 2.9(b), it consists of one layer of 90×60 $cm^2$ with 30 paddles, the paddles are 3×60×0.5 $cm^3$ and the time resolution is approximately of 20 ps (FWHM).

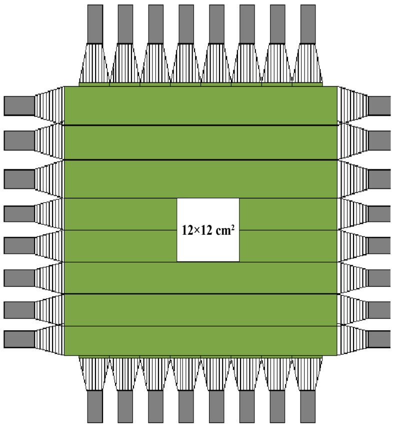


(a) Detector for light charged particles.

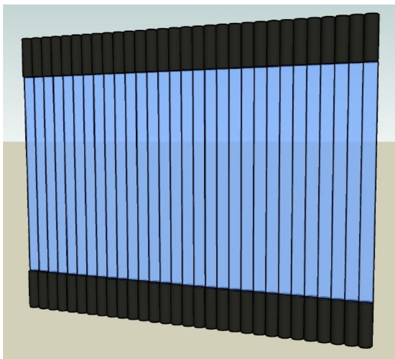

(b) ToF-wall for fission fragments.

***Figure 2.9:*** *ToF-walls for SOFIA experiment.*

### 2.1.6 The LAND detector

LAND is a **L**arge **A**rea **N**eutron **D**etector to study neutrons from near relativistic heavy ion collisions. LAND provides good spatial and momentum resolution. LAND has a front face of 2×2 $m^2$ and 1 m depth (see figure 2.10), it is subdivided in 200 independently operanting modules and 40 charged particle veto counter. The independently operanting modules are paddles of 200×10 $cm^2$ and 10 cm depth. Each paddle contains 11 sheets of iron (the two outer ones are 2.5 mm thick, the others are 5 mm thick) and 10 sheets of 5 mm thick scintillator, mounted in an iron sheet box which has a wall thickness of 1 mm. 20 paddles form a layer, subsequent layers have paddles perpendicular to each other, thus giving position information in both horizontal and vertical directions, orthogonal to the neutron incidence.

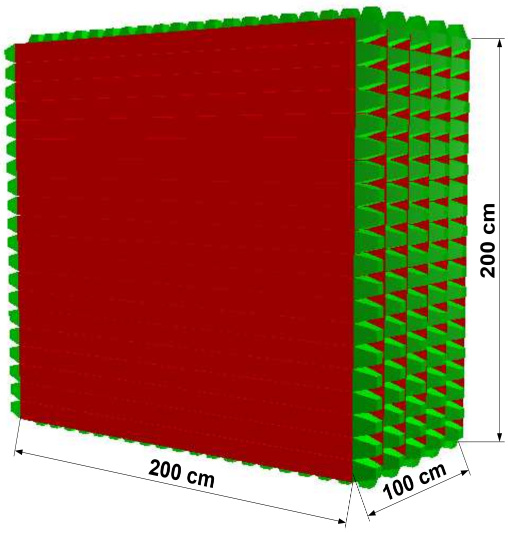


***Figure 2.10:*** *LAND detector.*

Ligth produced in a paddle is collected by means of ligth guides on both ends of the scintillator sheets and is directed to the photomultipliers, the difference in arrival time of the two signals serve to localize the interaction point position where scintillator light was produced by secondary charged particles. The mean time provides TOF information. A veto detector for charged particles is installed. The veto allows for identification of charged particles via ΔE-TOF analysis. It consists of two crossed layers, each with 20 scintillators strips, the strip size is of 200×10 cm$^2$ and 0.5 cm depth.

### 2.1.7 ALADIN dipole

ALADIN dipole has been employed in the simulation, it has a gap of 155×50×240 cm$^3$ filled with He in order to reduce the angular straggling and energy straggling. The iron constrains of the magnet and kapton windows have been also included in the simulation. It has been situated a 360 cm of target and rotated 7.0 degrees with respect to beamline. The figure 2.11 shows the form and dimensions of the gap and the figure 2.12 shows the Aladin magnetic field component in the $B_x$, $B_y$ and $B_z$ direction as a funtion of $r_x$, $r_y$ and $r_z$ direction. This field is obtained by interpolation of magnetic field measured at GSI for different currents.

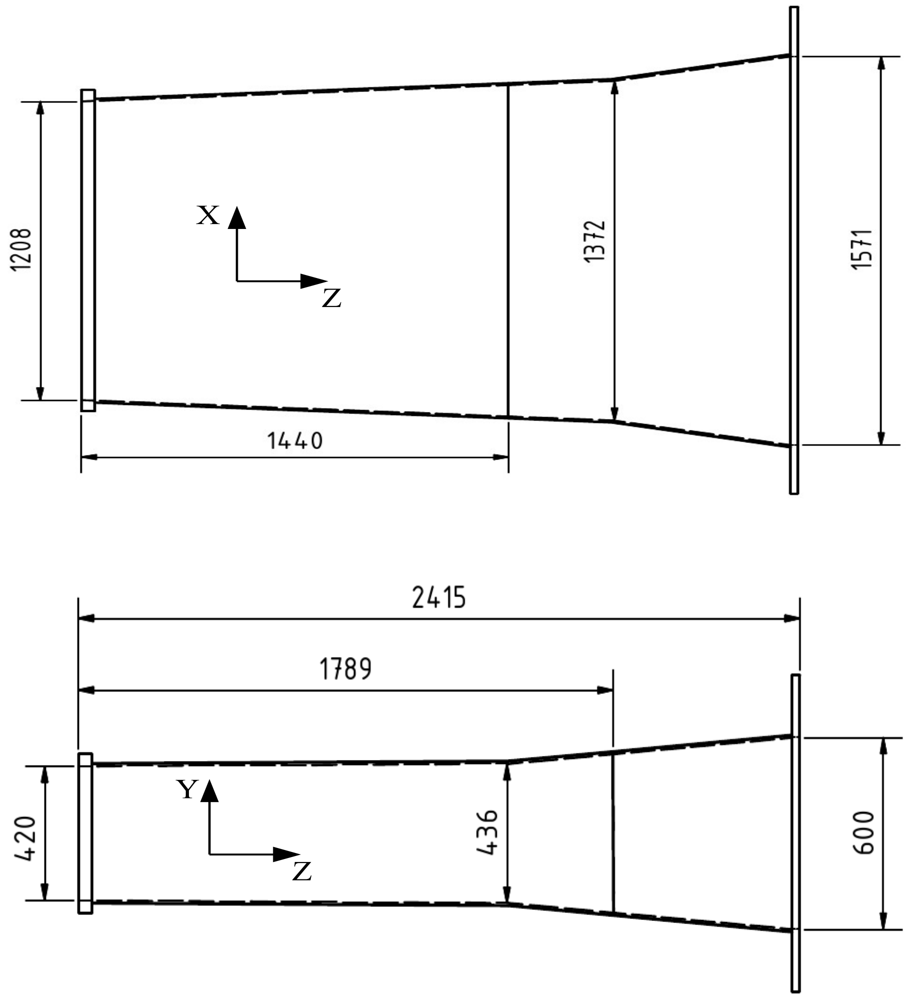


***Figure 2.11:*** *Dimensions of the gap in ALADIN dipole, all in mm.*

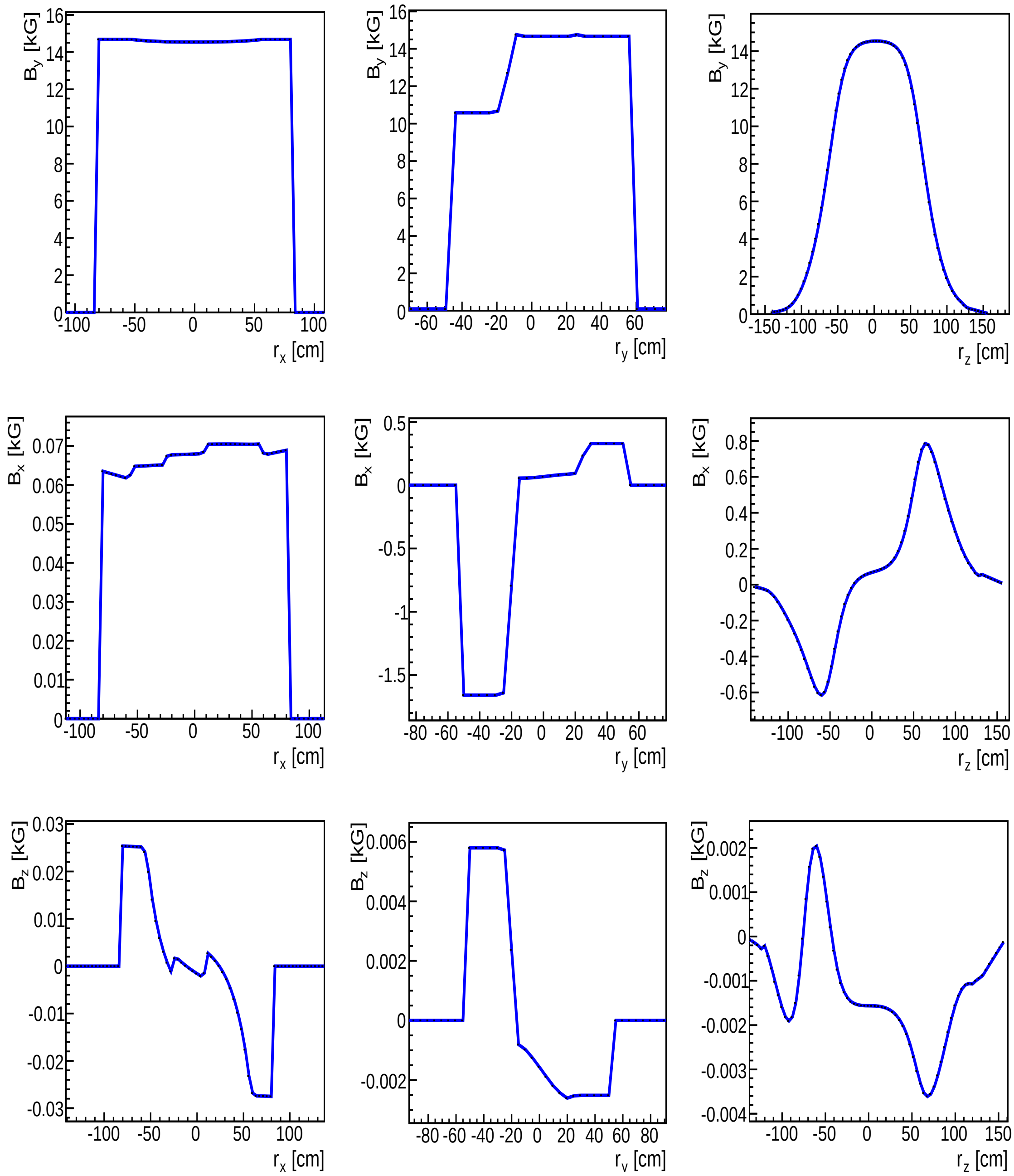


***Figure 2.12:*** *The Aladin magnetic field component in the $B_x$, $B_y$ and $B_z$ direction as a funtion the $r_x$, $r_y$ and $r_z$ direction (see figure 2.4). In the graph $B_y$ vs. $r_y$ we observe that the magnetic field is not symmetric but it is not important because the y dimension of Aladin is [-21, 21] cm.*

The figure 2.13 shows the acceptance for protons and $^{132}Sn$ at 500 A MeV and at 700 A MeV, for this we throw these from the target with three randoms, $\theta$, $\phi$ and kinetic energy and then we record the events that cross Aladin. If we plot B$\rho$ vs. $\theta$ of the particles we can see the acceptance as funtion of B$\rho$ or momentum of the particle.

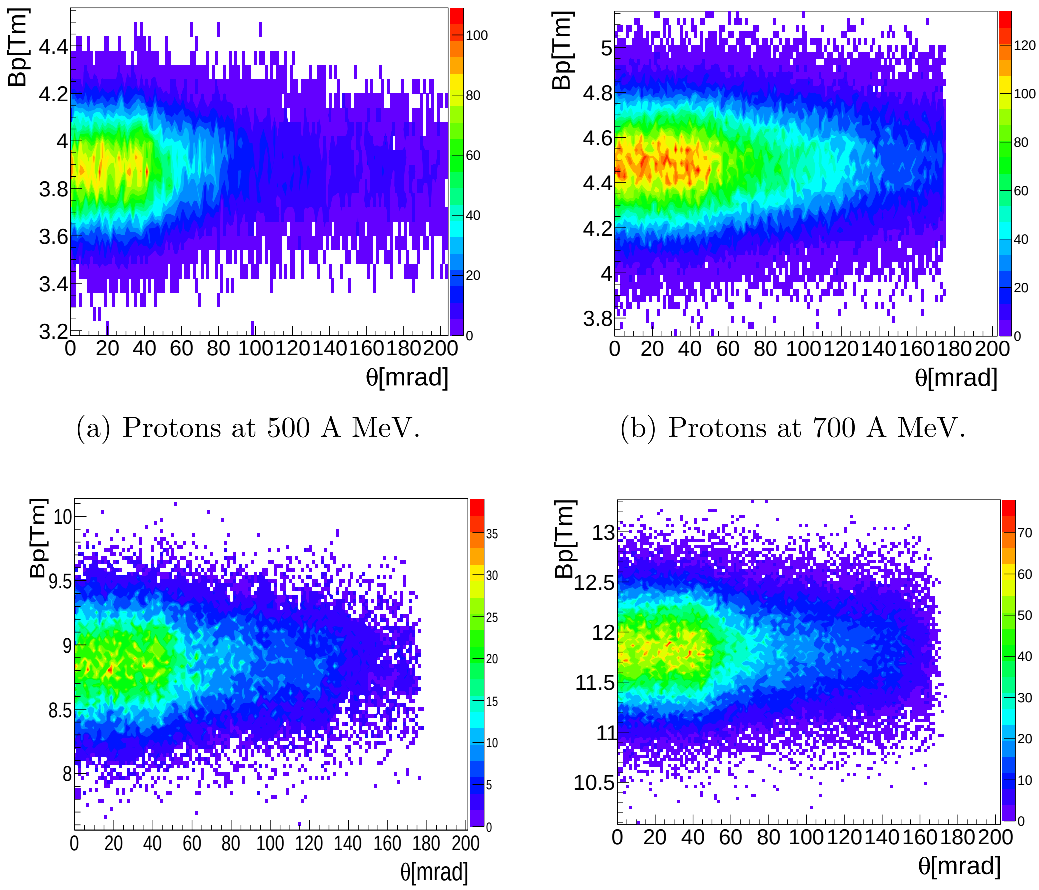


(a) Protons at 500 A MeV.

(b) Protons at 700 A MeV.

(c) $^{132}Sn$ at 500 A MeV.

(d) $^{132}Sn$ at 700 A MeV.

***Figure 2.13:*** *B$\rho$ vs. $\theta$ for different ions at 500 A MeV and 700 A MeV. It shows the ALADIN acceptance.*

# Chapter 3

# Description of the simulation

The present simulations use the interface of R3BRoot [5] which is the simulation and analysis framework for the R3B experiment. It is based on the FairRoot library [6] which is used in many experiments at FAIR. It provides a common data structure for simulation and analysis based on Root trees, a detector geometry description based on the Root Geometry Modeller and an interface to different Monte Carlo engines using the Root Virtual Monte Carlo package. It allows to perform simulation using Geant3, Geant4 [7] or Fluka. In our case we have used Geant4. In adittion ABRABLA [8] code and INCL [9]+ABLA [10] code have been used to simulate the production and the kinematic of the fission fragments and light charged particles produced in the reactions that will be investigated with the SOFIA experiment. In this chapter we will briefly present and validate the different codes we have used to simulate the SOFIA experiment.

## 3.1 Reaction codes: INCL+ABLA and ABRABLA

The nuclear reaction Monte-Carlo code, INCL+ABLA, has been used to simulate the raction p+$^{208}$Pb at 500 A MeV. The reactions between two nuclei at relativistic energies can be described as two subsequent steps. In the first cascade stage, the proton interacts with the target very fast about $10^{-23}$ s and introduce a certain amount of excitation energy in the system. During the second slow stage $10^{-16}$-$10^{-20}$ s the projectile residue thermalizes and decays to ground state nuclei by particle evaporation or fission. The first part of the reaction is simulated by the INCL code and the second part of the ABLA code.

The nuclear reaction Monte-Carlo code, ABRABLA, has been used to simulate the nucleus-nucleus collisions at relativistic energies (collision $^{238}$U+$^{238}$U). This is an abrasion-ablation model developed at GSI. In the first stage of the collision, abrasion, projectile and target nuclei loss nucleons according to geometrical considerations and gain excitation energy. This excitation energy is consumed in the ablation process. The de-excitation is described by the statistical model, where the evaporation of nucleons and fission are competitive processes. The calculation of the probability for one or other channel is based on statistical considerations connected to the number of available phase space for the nucleus. If the nucleus reaches the fission, the fission fragments can have some excitation energy and can evaporate some nucleons.

The characteristics of the fission fragments are described with a semi-empirical Monte-Carlo code developed to calculate the mass and charge distributions of fission fragments. In the model, for a given excitation energy E*, the yield of the fission fragments with neutron number N, Y(E*, N), is determined by the number of available transition states above the mass asymmetry potential energy at the fission barrier. It is assumed that the mass-asymmetric degree of freedom at the fission barrier is on average uniquely related to the neutron number N of the fission fragments. The number of protons and neutrons are considered to be correlated. The barrier as function of the mass asymmetry is defined by three components. The symmetric component, defined by the liquid-drop potential, is described by a parabola. The other components are the asymmetric channels, which are known as "standard I" and "standard II" and represent shell effects. The excitation energies of the fragments are calculated from the excitation and deformation energy of the fissioning system at the scission point.

In addition, the kinematics of the fission process is treated inside of this subroutine. The mean velocity of fission fragments can be estimated by the following empirical description of the total kinetic energy known also as Wilkins model

$$TKE = \frac{Z_1 Z_2 e^2}{D} \;\; with \;\; D = r_0 A_1^{1/3}\left(1+\frac{2\beta_1}{3}\right) + r_0 A_2^{1/3}\left(1+\frac{2\beta_2}{3}\right) + d \quad (3.1)$$

where $A_1$, $A_2$, $Z_1$, $Z_2$ denote the mass and charge numbers of a pair of fission fragments prior to neutron evaporation. D represents the distance between the two nuclei and is given by the fragments radius ($r_0 A^{1/3}$), corrected for the deformation ($\beta$), plus the neck (d). The parameters ($r_0$=1.16 fm, d=2.0 fm, $\beta_1 = \beta_2 = 0.625$) were deduced from experimental data in ref. [11] and are consistent with values previously found in the analysis of ref. [12].

The INCL+ABLA and ABRABLA codes generate a file with the momentum of the fission fragments which are included in Geant4 to perform the simulation. The validation of the kinematics calculations is shown in figures 3.1 and 3.2.

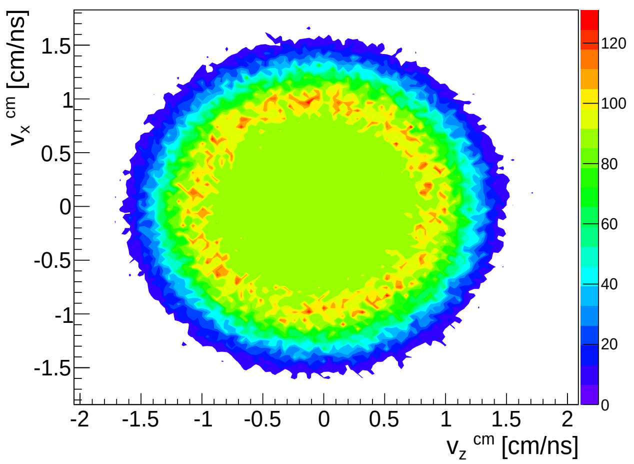


***Figure 3.1:*** *$V_x^{cm}$ vs. $V_z^{cm}$ velocity for fission fragments produce in INCL+ABLA code for the collision p+$^{238}$U.*

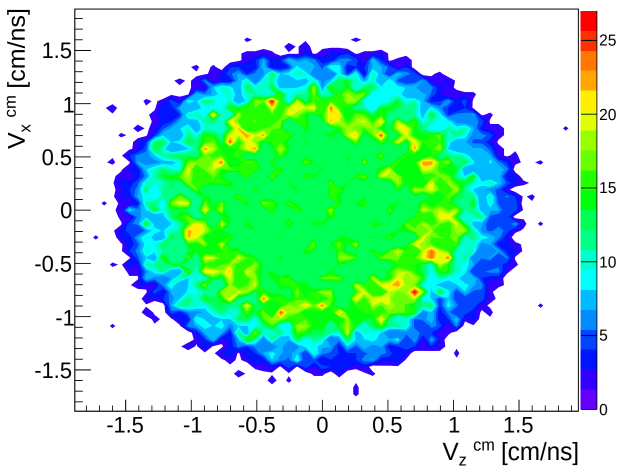


***Figure 3.2:*** *$V_x^{cm}$ vs. $V_z^{cm}$ velocity for fission fragments produce in ABRABLA code for the collision $^{238}$U+$^{238}$U.*

## 3.2 The AMADEUS code

AMADEUS (**A MA**gnet and **DE**grader **U**tility for **S**caling) is a program developed at GSI. AMADEUS [13] performs quick calculations of deflection of high-energetic heavy ions in magnetic spectrometers, slowing down nuclear reactions in the different layers of matter, and also relativistic kinematical transformations. The validity range of the models used for the calculations is tested in the energy range between 50 MeV/A and 1,5 GeV/A. The agreement between calculated energy loss and measured data is in the order of 4%.

## 3.3 The Geant4 code

### 3.3.1 Introduction

Geant4 (for **GE**ometry **AN**d **T**racking) is a code to simulate the interactions of particles and ions with matter, in an energy range between 35 keV and a few TeV. This code can simulate a complete experiment, with all its detectors and the particle propagation. The step length for the particle propagation is defined internally by the program taking into account the energy of the paticle, the traversed materials and possible interactions that the particle can have. Geant4 has several libraries to simulate the interaction of particles with matter, in this simulation the most common libraries used are G4hIonisation, G4ionIonisation, G4hMultipleScattering and G4MultipleScattering. These allow us to simulate the energy loss of hadrons (G4hIonisation) and ions (G4ionIonisation), as well as their angular straggling (G4hMultipleScattering and G4MultipleScattering). There are other libraries that are loaded by default, these can be seen in Appendix A.

We must check that Geant4 simulates correctly the energy loss, energy straggling and angular straggling to ensure that our results are correct. For this we simulate the collision of different projectiles with different targets, these results are compared with results from AMADEUS and with experimental results [14].

### 3.3.2 Energy loss

The energy loss can be expressed by the well know Bethe-Bloch expression for the stopping power of heavy particles

$$-\frac{dE}{dx} = \frac{4\pi N Z^2 e^4}{m_e \beta^2 c^2} \left[ ln\left(\frac{2m_e\beta^2c^2}{I}\right) - ln(1-\beta^2) - \beta^2 \right] \quad (3.2)$$

where N is the number od electors per volumen unit, Z and $\beta$ are the charge and velocity of the projectile, respectively, and I is the ionisation potencial of the target.

But the Bethe-Bloch expression 3.2 becomes invalided when dealing with particles of high atomic charge because of the failure on the first Born approximation. In order to know precisely the stopping power for heavy ions, Ahlen presented a formalism that takes into account additional terms in the energy loss expression that become important when the charge of the projectile increases. He introduced terms to account for the exact Mott cross section for scattering, the electron binding energy during close collisions, Bloch scattering and relativistic Bloch scattering. These terms can be described as a series of terms of higher power of the charge of the projectile. The energy loss can be written as

$$-\frac{dE}{dx} = \frac{4\pi N e^4}{m_e c^2} \frac{Z_{pe}^2}{\beta^2} \left[ ln\left(\frac{2m_e\beta^2c^2}{I(1-\beta^2)}\right) - \beta^2 - S - D - M - B \right] \quad (3.3)$$

where $Z_{pe}$ is the projectile effective charge that is different the true atomic number, it can be expressed by the semiempirical formula 3.4 which is drawn for different ions in the figure 3.3

$$Z_{pe} = Z\left[1 - exp\left(\frac{-130\beta}{Z^{2/3}}\right)\right] \quad (3.4)$$

The corrections that appear in the equation 3.3 are:

- S is the correction fo shell effects introduced by Barkas and Berger. It takes into account that at projectile velocities comparable or even smaller than the orbital velocities of the bound target electrons the energy transfer is less effective. This contribution decreases with $1/\beta^2$, for relativistic ions even the contribution to the stopping power from the interactions with the target K-shell electrons is affected very litte and shell corrections can safely be ignored.

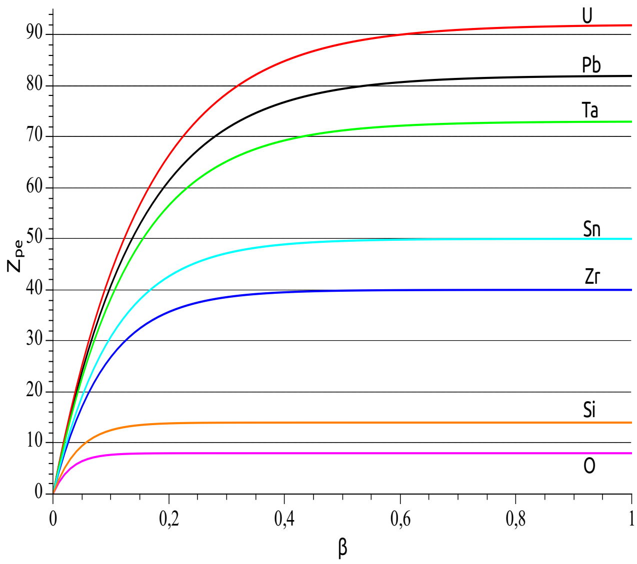


***Figure 3.3:*** *Zpe as funtion of* $\beta$ *for different ions.*

- D is the relativistic density correction introducted by Fermi. If the target medium is not a dilute gas but the density of atoms is high, the projectile charge is screened by dielectric polarization of the medium and the energy transfer in large impact parameters collisions is less effective. This contribution is not significant to the stopping power calculations if $\beta \leq 0.88$.

- M is the correction for Mott scatering, for large nuclear charges the scattering cross section in Born approximation differs significantly from the exact cross section. An exact solution of the Dirac equation for the scattering of a relativistic electron in the central field of a point nucleus was first given by Mott.

- B is a correction derived by Bloch for electron binding during close collisions.

In Geant4, the energy loss process must calculate the continuous and discrete energy loss in a material. Below a given energy threshold the energy loss is continuous and above it the energy loss is simulated by the explicit production of secondary particles: gammas, electrons, and positrons. If we take

$$\frac{d\sigma(Z,E,T)}{dT} \tag{3.5}$$

the differential cross-section per atom (atomic number Z) for the ejection of a secondary particle with kinetic energy T by an incident particle of total energy E moving in a material of density $\rho$. The value of the kinetic energy cut-off or production threshold is denoted by $T_{cut}$ . Below this threshold the soft secondaries ejected are simulated as continuous energy loss by the incident particle, and above it they are explicitly generated. The mean rate of energy loss is given by:

$$\frac{dE(E, T_{cut})}{dx} = n_{at} \int_0^{T_{cut}} \frac{d\sigma(Z, E, T)}{dT} T dT \tag{3.6}$$

where $n_{at}$ is the number of atoms per volume in the material. If there are several processes providing energy loss for a given particle, then the total continuous part of the energy loss is the sum:

$$\frac{dE^{tot}(E, T_{cut})}{dx} = \sum_i \frac{dE_i(E, T_{cut})}{dx} \tag{3.7}$$

The integration of 3.6 leads to the Bethe-Bloch restricted energy loss ($T < T_{cut}$), which is modified taken into account various corrections:

$$-\frac{dE}{dx} = 2\pi r_e^2 m_e c^2 n_{el} \frac{Z_{pe}^2}{\beta^2} \left[ ln \left( \frac{2m_e c^2 \beta^2 \gamma^2 T_{up}}{I^2} \right) - \beta^2 \left( 1 + \frac{T_{up}}{T_{max}} \right) - \delta - \frac{2C_e}{Z} + F \right] \tag{3.8}$$

where $T_{up}$ is the minimum of ($T_{cut}$, $T_{max}$) and $n_{el}$ is the electrons density in the material

$$n_{el} = Z n_{at} = Z \frac{N_{av} \rho}{A} \tag{3.9}$$

where $N_{av}$ is Avogadro number, $\rho$ is the density of the material and A is the mass of a mole.

The term $2C_e/Z$ is the shell correction, $\delta$ is the density effect term and F is the high order corrections term, which is expressed as

$$F = G - S + 2(Z_p L_1 + Z_p^2 L_2) \tag{3.10}$$

where G is the Mott correction term, S is the finite size correction term, $L_1$ is the Barkas correction, $L_2$ is the Bloch correction. The Mott term describes the close-collision corrections tend to become more important at large velocities and higher charge of projectile. The Fermi result is used

$$G = \pi \alpha Z_p \beta \tag{3.11}$$

The energy loss is calculated to each step, which is expressed as

$$\Delta T = \frac{dE}{dx}\Delta s \tag{3.12}$$

where $\Delta s$ is the step length.

The AMADEUS code is based on a semiempirical algorithm to evaluate energy loss in thick layers following a fast and efficient procedure. The basic idea is to parameterised the range of ions in some material by using an analytical function that can be inverted. The energy loss in a layer of matter with thickness s can be obtained as

$$\Delta E(s) = E_i - E_f \tag{3.13}$$

where $E_i$ and $E_f$ are the initial energy of ion and the final energy of ion after crossing the layer of matter, respectively. The $E_f$ can be easily be calculated from the residual ranges before and behind the layer, r($E_i$) and r($E_f$), used

$$r(E_f) = r(E_i) - s \tag{3.14}$$

where r(E) is a function that can be inverted. To determine the funcion r(E) the range of a number of different projectile stopper combinations was calculated by numerical integrations of the stopping power expressions. Then, the values were fit with the least-squares method, in an energy range between 100 A MeV and 2 A GeV, to the function

$$r(Z_p, A_p, E/A_p) = \kappa\frac{A_p}{Z_p^2}10^{\kappa} \quad mg/cm^2 \tag{3.15}$$

where $A_p$ and $Z_p$ are the mass and atomic number of the ion, respectively, and E/$A_p$ is the energy in A MeV. The parameter $\kappa$ is polinomial and logarithm combination of different powers in $Z_p$ and E/$A_p$. The expression 3.15 can be inverted to get the energy as a function of the residual range of the ion. Using this method, AMADEUS code computes the energy loss in one step and it does not need to integrate any stopping power expression.

These codes have different equations but the results (see figures 3.4, 3.5, 3.6 and Appendix B) show an agreement of the order of 2.16% for Geant4 and the 3.1% for AMADEUS. In principle, these results allows us to validate the energy loss caculations obtained with Geant4 in the range of ions and energies of interest for the SOFIA experiment.

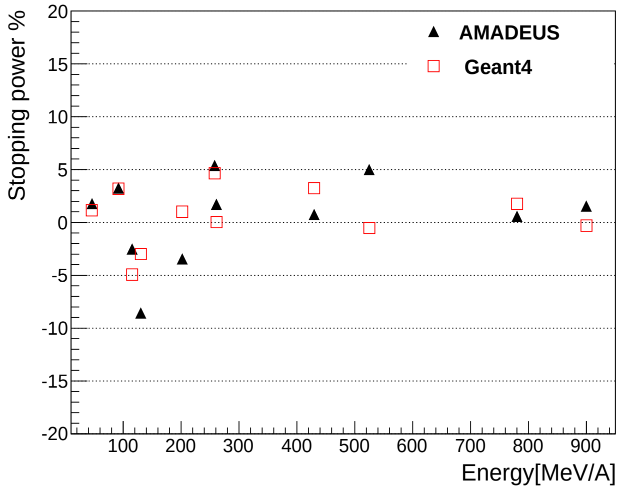


***Figure 3.4:*** *Beryllium target: Percentual difference between experimental and calculated stopping power with AMADEUS and the difference between experimental and calculated stopping power with Geant4 as a funtion of the incident ion energy per nucleon.*

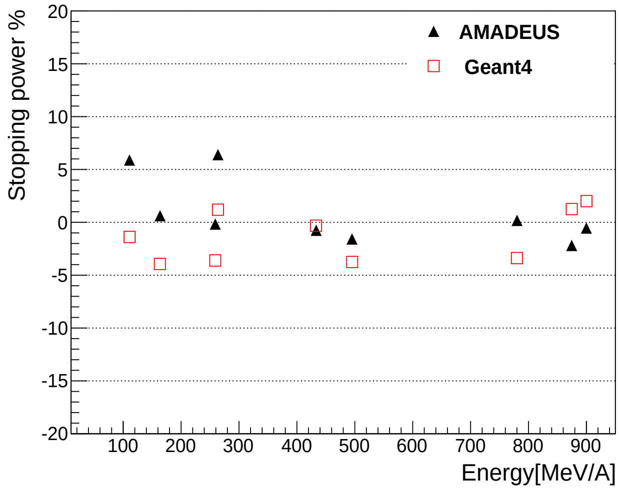


***Figure 3.5:*** *Cooper target: Percentual difference between experimental and calculated stopping power with AMADEUS and the difference between experimental and calculated stopping power with Geant4 as a funtion of the incident ion energy per nucleon.*

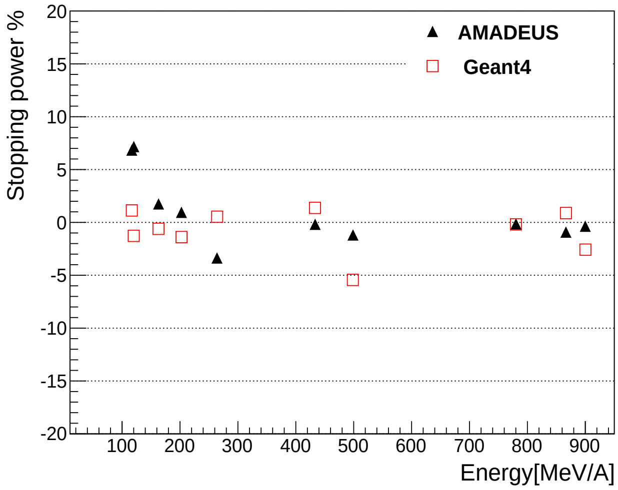


***Figure 3.6:*** *Aluminium target: Percentual difference between experimental and calculated stopping power with AMADEUS and the difference between experimental and calculated stopping power with Geant4 as a funtion of the incident ion energy per nucleon.*

### 3.3.3 Energy straggling

The total continuous energy loss of charged particles is a stochastic quantity with a distribution described in terms of a straggling function. When ions penetrate matter, the statistical fluctuations of the impact parameters as well as the variation of the transferred momentum in the scattering cause a fluctuation in the energy loss distribution.

In Geant4, the straggling is partially taken into account by the simulation of energy loss by the production of $\delta$-electrons with energy T $> T_c$. However, continuous energy loss also has fluctuations. Hence in the current GEANT4 implementation two different models of fluctuations (thick absorbers and thin absorbers) are applied depending on the value of the parameter $\kappa$ which is the lower limit of the number of interactions of the particle in the step. The default value chosen is $\kappa = 10$. To select a model for thick absorbers the following boundary conditions are used:

$$\Delta E > \kappa T_c \ \ or \ \ T_c < I\kappa \tag{3.16}$$

where $\Delta E$ is the mean continuous energy loss in a track segment of length s, $T_c$ is the cut kinetic energy of $\delta$-electrons, and I is the average ionisation potential of the atom. In the case of thick absorbers, for long path lengths the straggling function approaches the Gaussian distribution with Bohr′s variance:

$$\Omega^2 = KN_{el}\frac{Z_h^2}{\beta^2}T_c s f\left(1-\frac{\beta^2}{2}\right) \tag{3.17}$$

where the factor K is expressed as K $= 2\pi r_e^2 m_e c^2$ (where $r_e$ is the classical electron radius), $N_{el}$ is the electron density of the medium, $Z_h$ is the effective charge of the incident particle, $\beta$ is the relativistic velocity and f is a screening factor, which is equal to unity for fast particles, whereas for slow positively charged ions with $\beta^2 <$ 3Z($v_0$ /c)$^2$ f = a + $b/Z_{eff}^2$ , where parameters a and b are parametrised for all atoms.

If the conditions 3.16 are not satisfied, the case of thin absorbers is applied. The formulas used to compute the energy loss fluctuation are based on a very simple physics model of the atom. It is assumed that the atoms have only two energy $E_1$ and $E_2$. The particle-atom interaction can be an excitation with energy loss $E_1$ or $E_2$, or ionisation with energy loss distributed according to a function g(E) $\sim 1/E^2$. The mean energy loss in a step is the sum of the excitation and ionisation contributions and can be written as

$$\frac{dE}{dx}\Delta E = \left(\Sigma_1 E_1 + \Sigma_2 E_2 + \int_{E_0}^{Tup} E g(E) dE\right)\Delta x \tag{3.18}$$

where the $\Sigma_i$ is the macroscopic cross section for each excitation energy, $E_0$ is the ionisation energy of the atom and $T_{up}$ is the threshold for delta ray production.

AMADEUS assumes that the materials have a sufficient thickness as to assume that the energy loss follows a Gaussian distribution. The $\Omega$ can be written as:

$$\Omega = 0.0089\left(\frac{E_i}{E_f}\right)^{1/3}\frac{Z_p}{A_P}\sqrt{\frac{Z_t}{A_t}X(\delta^2+1)} \tag{3.19}$$

where $Z_p$, $Z_t$, $A_p$ and $A_t$ are the masico number and atomic number for the projectil and the target. X is the material thickness in $mg/cm^2$ and $\delta$ depend the entrance and exit energy, it is given by the expression

$$\delta = 1 + \frac{E_i + E_f}{1863} \tag{3.20}$$

In this case the results (see tables 3.1, 3.2 and 3.3) do not show a too good agreement but this is not crucial because these energies represents 0.02% of the total kinetic energy.

| E(MeV/A) | Proj. | Amadeus | Geant4 |
|---|---|---|---|
| 130.7 | $^{208}$Pb† | 10.65 | 50.0 |
| 201.8 | $^{208}$Pb† | 10.62 | 39.11 |
| 257.7 | $^{197}$Au† | 10.41 | 32.34 |
| 261 | $^{58}$Ni* | 1.4 | 1.15 |
| 430 | $^{58}$Ni† | 3.96 | 3.93 |
| 470 | $^{208}$Pb† | 11.88 | 28.99 |
| 500 | $^{208}$Pb† | 10.05 | 28.62 |
| 525.1 | $^{209}$Bi† | 29.16 | 12.34 |
| 630 | $^{208}$Pb† | 12.80 | 27.31 |
| 690 | $^{18}$O† | 1.28 | 1.26 |
| 780 | $^{136}$Xe† | 9.01 | 8.95 |
| 900 | $^{238}$U† | 16.20 | 33.59 |

***Table 3.1:*** *Energy straggling for beryllium target (* 0.01 cm and † 0.1 cm thickness). The energy straggling are measured in MeV.*

| E(MeV/A) | Proj. | Amadeus | Geant4 |
|---|---|---|---|
| 110.9 | $^{197}$Au* | 10.18 | 57.82 |
| 163.3 | $^{209}$Bi* | 7.33 | 37.07 |
| 258.8 | $^{209}$Bi* | 7.61 | 52.50 |
| 263.4 | $^{197}$Au† | 25.27 | 96.84 |
| 433 | $^{136}$Xe* | 5.39 | 10.02 |
| 470 | $^{208}$Pb† | 27.19 | 81.13 |
| 495.2 | $^{209}$Bi* | 8.56 | 24.78 |
| 530 | $^{208}$Pb† | 27.82 | 75.23 |
| 580 | $^{208}$Pb† | 28.38 | 75.23 |
| 630 | $^{208}$Pb† | 28.38 | 71.98 |
| 780 | $^{136}$Xe† | 20.23 | 19.79 |
| 874.7 | $^{209}$Bi* | 10.19 | 10.05 |
| 900 | $^{238}$U* | 11.42 | 27.92 |

***Table 3.2:*** *Energy straggling for copper target (* 0.01 cm and † 0.1 cm thickness). The energy straggling are measured in MeV.*

| E(MeV/A) | Proj. | Amadeus | Geant4 |
|---|---|---|---|
| 117 | $^{197}$Au† | 13.76 | 75.23 |
| 120.4 | $^{208}$Pb† | 14.21 | 78.94 |
| 162.8 | $^{209}$Bi† | 13.81 | 65.99 |
| 202.6 | $^{208}$Pb† | 13.58 | 57.62 |
| 264 | $^{58}$Ni* | 1.45 | 1.75 |
| 433 | $^{136}$Xe* | 3.04 | 5.29 |
| 498.6 | $^{209}$Bi† | 15.39 | 40.89 |
| 530 | $^{208}$Pb† | 15.43 | 39.25 |
| 590 | $^{208}$Pb† | 15.85 | 38.83 |
| 690 | $^{18}$O† | 1.61 | 1.60 |
| 780 | $^{136}$Xe† | 11.36 | 11.34 |
| 866.7 | $^{209}$Bi* | 5.72 | 5.69 |
| 900 | $^{238}$U† | 20.41 | 47.76 |

***Table 3.3:*** *Energy straggling for aluminium target (* 0.01 cm and † 0.1 cm thickness). The energy straggling are measured in MeV.*

### 3.3.4 Angular straggling

When the charged particles crossing the matter, in addition the collisions with the atomic electrons, suffer elastic Coulomb scattering. Ignoring spin effects, these collisions can be described by the well known Rutherford formula

$$\frac{d\sigma}{d\Omega} = z^2 Z^2 r_e^2 \frac{mc/\beta p}{4sin^4(\theta/2)} \tag{3.21}$$

where z is the charge of the projectile, Z is the charge of the target, $r_e$ is the Bohr radius, m, p and $\beta$ are the mass, momentum and velocity of the projectil, respectively. $\theta$ is the deflection angle from initial trayectory. The majority of these collisions result in a small angular deflection of the particle. The particle follows a random path inside the matter and the cumulative effect of these small angle scattering results in a total angle of deflection from the original particle direction. In adittion, if the average number of independent scattering events is large and the energy loss in each collision is small or negligible, we can say that the particle has suffered multiple scattering (the strong interactions also can contribute to multiple scattering). Rigurous caculations of multiple scattering are extremely complicated and there exist several formulations with different sofistication levels, the most commonly used is the small angle approximation of Moliere.

In us case, we can use the multiple scattering gaussian approximation, ignoring the small probability of large angle single scattering. According to this, a very good estimation of the gaussian width is obtained using an empirical formula proposed by Highland [15]

$$\theta = \frac{20[MeV/c]}{p\beta} z \sqrt{\frac{x}{X_0}} \left[1 + \frac{1}{9} log_{10}\left(\frac{x}{X_0}\right)\right] \tag{3.22}$$

where z, p and $\beta$ are the charge, momentum and velocity of the projectil, respectively. x $[cm]$ is the thickness of material and $X_0$ is the radiation length.

In Geant4, the Highland formula is used, but modified as follows

$$\theta = \frac{13.6MeV}{\beta cp} z \sqrt{\frac{t}{X_0}} \left[1 + 0.105 ln\left(\frac{t}{X_0}\right) + 0.0035\left(ln\left(\frac{t}{X_0}\right)\right)^2\right]^{1/2} f(z) \tag{3.23}$$

where t is the true step length and f(z) is an empirical correction factor.

$$f(z) = 1 - \frac{0.24}{z(z+1)} \tag{3.24}$$

The AMADEUS code computes the angular straggling with the Highland expression, but modified as follows

$$\theta = \frac{14.1}{\sqrt{\beta_i p_i \beta_f p_f}} z \sqrt{\frac{X}{X_0}} \left(1 + \frac{1}{9} log_{10}\left(\frac{X}{X_0}\right)\right) \tag{3.25}$$

where $\beta_i$, $p_i$, $\beta_f$, $p_f$ are the velocity and momentum before and after crossing the matter, respectively. The radiation lenght is computed as

$$X_0 = \frac{716.405}{Z^2} \left[ln\left(\frac{184.15}{Z^{1/3}}\right) - 1.202\alpha^2 Z^2 + 1.0369 Z^4 - \frac{1.008\alpha^6 Z^6}{1 + \alpha^2 Z^2}\right] \tag{3.26}$$

| E(MeV/A) | Proj. | Amadeus | Geant4 |
|---|---|---|---|
| 46 | $^{58}$Ni$*$ | 0.794 | 0.811 |
| 92 | $^{58}$Ni$*$ | 0.398 | 0.414 |
| 115.3 | $^{197}$Au† | 1.144 | 1.138 |
| 130.7 | $^{208}$Pb† | 0.969 | 0.884 |
| 201.8 | $^{208}$Pb† | 0.608 | 0.592 |
| 257.7 | $^{197}$Au† | 0.486 | 0.496 |
| 261 | $^{58}$Ni* | 0.150 | 0.158 |
| 430 | $^{58}$Ni† | 0.361 | 0.366 |
| 470 | $^{208}$Pb† | 0.275 | 0.261 |
| 500 | $^{208}$Pb† | 0.250 | 0.240 |
| 525.1 | $^{209}$Bi† | 0.251 | 0.254 |
| 630 | $^{208}$Pb† | 0.213 | 0.203 |
| 690 | $^{18}$O† | 0.220 | 0.220 |
| 780 | $^{136}$Xe† | 0.185 | 0.185 |
| 900 | $^{238}$U† | 0.154 | 0.142 |

***Table 3.4:*** *Angular straggling for beryllium target (* 0.01 cm and † 0.1 cm thickness). The angular straggling are measured in mrad.*

| E(MeV/A) | Proj. | Amadeus | Geant4 |
|---|---|---|---|
| 110.9 | $^{197}$Au* | 2.84 | 2.61 |
| 163.3 | $^{209}$Bi* | 1.21 | 1.25 |
| 258.8 | $^{209}$Bi* | 0.78 | 0.79 |
| 263.4 | $^{197}$Au† | 3.28 | 3.23 |
| 433 | $^{136}$Xe* | 0.49 | 0.49 |
| 470 | $^{208}$Pb† | 1.73 | 1.70 |
| 495.2 | $^{209}$Bi* | 0.44 | 0.45 |
| 530 | $^{208}$Pb† | 1.55 | 1.53 |
| 580 | $^{208}$Pb† | 1.42 | 1.46 |
| 630 | $^{208}$Pb† | 1.32 | 1.31 |
| 780 | $^{136}$Xe† | 1.09 | 1.11 |
| 874.7 | $^{209}$Bi* | 0.27 | 0.28 |
| 900 | $^{238}$U* | 0.26 | 0.26 |

***Table 3.5:*** *Angular straggling for copper target (* 0.01 cm and † 0.1 cm thickness). The angular straggling are measured in mrad.*

| E(MeV/A) | Proj. | Amadeus | Geant4 |
|---|---|---|---|
| 117 | $^{197}$Au† | 2.65 | 2.55 |
| 120.4 | $^{208}$Pb† | 2.51 | 2.27 |
| 162.8 | $^{209}$Bi† | 1.73 | 1.58 |
| 202.6 | $^{208}$Pb† | 1.35 | 1.32 |
| 264 | $^{58}$Ni* | 0.33 | 0.32 |
| 433 | $^{136}$Xe* | 0.17 | 0.18 |
| 498.6 | $^{209}$Bi† | 0.58 | 0.55 |
| 530 | $^{208}$Pb† | 0.54 | 0.54 |
| 590 | $^{208}$Pb† | 0.49 | 0.50 |
| 690 | $^{18}$O† | 0.48 | 0.47 |
| 780 | $^{136}$Xe† | 0.39 | 0.37 |
| 866.7 | $^{209}$Bi* | 0.10 | 0.10 |
| 900 | $^{238}$U† | 0.34 | 0.34 |

***Table 3.6:*** *Angular straggling for aluminium target (* 0.01 cm and † 0.1 cm thickness). The angular straggling are measured in mrad.*

The expressions used in the two codes to calculate the angular straggling are differents but the both results (see tables 3.4, 3.5 and 3.6) are very similar, which allows us again to validate the estimations of the angular straggling obtained with Geant4.

# Chapter 4

# Results of the simulation

In this chapter we will present the main results obtained with the simulation code conccernig the detection efficiency of fission fragments, neutrons and light-charged particles and the reconstruction of the mass of the fission fragments. For the two reactions investigated in SOFIA experiment, $^{238}$U+$^{238}$U and $^{208}$Pb+p, we have simulated 1200 events using a cluster of computers (64 cores, Processor AMD Opteron) with a processing time of 3 hours.

## 4.1 Detection efficiency

### 4.1.1 Simulation of the reaction conditions

In the case of the $^{238}$U experiment, the primary beam will reach the Cave C at 700 A MeV, however one has to take into account the energy loss of Uranium before reaching the target. As a correction, we simulate the energy loss of Uranium in the air and all the detectors placed in front of the target (TPCs, TUM MUSICs and start scintillator) with the code AMADEUS (see Appendix C). Equations 4.1, 4.2 and 4.3 represent the energy (in A MeV) of $^{238}$U beam in the middle of each layer of the active target as funtion of the longitudinal position (z). (see figure 2.7).

$$E(U1) = 586.090 - 997.895z\ (cm) \tag{4.1}$$

$$E(Pb) = 550.395 - 647.82z\ (cm) \tag{4.2}$$

$$E(U2) = 513.671 - 1039.63z\ (cm) \tag{4.3}$$

In the case of the $^{208}$Pb beam the energy is 560 A MeV when it reaches the Cave C and once again one has to take into account the energy loss before reaching the target (see Appendix C). Equation 4.4 shows the energy (in A MeV) of the $^{208}$Pb beam in the middle target as funtion of the longitudinal position (z).

$$E = 500.613 - 13.034z\ (cm) \tag{4.4}$$

Then, we generate with ABRABLA and INCL+ABLA codes the file with the velocity, mass and atomic numbers of the fission fragments in the CM system for the collisions $^{238}$U+$^{238}$U and $^{208}$Pb+p, respectively. Then we apply the Lorentz boost to calculate the velocities in the laboratory system as

$$v_z^{lab} = \frac{\beta + v_z^{cm}}{1 + \frac{\beta \cdot \mathbf{v^{cm}}}{c^2}} \qquad v_{x,y}^{lab} = \frac{v_{x,y}^{cm}}{\gamma \left(1 + \frac{\beta \cdot \mathbf{v^{cm}}}{c^2}\right)} \tag{4.5}$$

where $\beta$ is the Lorentz boost velocity. Finally we calculate the momentum as $P_i = M \cdot v_i^{lab}$ where M is the mass of the particle or ion.
In the case of collisions $^{238}$U+$^{238}$U we use the active target, so we randomly sample in which of the three targets the reaction takes place and the longitudinal and perpendicular reaction position in the target. The perpendicular beam spot is considered as a circle with 1 cm diameter. From the longitudinal reaction position (z) we determine from equations 4.1, 4.2 and 4.3 the energy of the incoming projectile, which is used by the Lorentz boost.
In the case of collision $^{208}$Pb+p, we sample the fission fragments according to two randoms, the longitudinal and perpendicular reaction position in the target. In this case the perpendicular beam spot is considered as a circle with 4 mm diameter. From the longitudinal reaction position (z) we determine using equations 4.4 the energy of the incoming projectile, which is used by the Lorentz boost.

### 4.1.2 Detection efficiency of fission fragments

One important result is to know the dispersion and the position of the fission fragments on the Tof-wall and the second MWPC (after ALADIN, see figure 2.4) since these positions will determine our geometrical efficiency. For this purpose, we simulate 12000 fission events for the collision $^{238}$U+$^{238}$U with the ABRABLA code. The results of the propagation are shown in figure 4.1. One can see that the dispersion is 80 cm in X direction (see figure 4.1(a)) and 70 cm in Y direction (see figure 4.1(b)). Therefore we lose some fission fragments because our detector surface[1] (MWPC) is 90×60 cm$^2$, being the corresponding efficiency 89 %. These calculations have been done with the detectors in the position X=-80 cm, Z= 695 cm and rotated 7°.

[1] In principle we change the dimensions of our detector to get the total dispersion of the fission fragments.

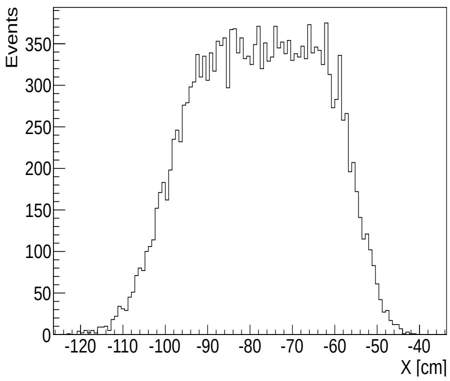


(a) X position for fission fragments in the second MWPC.

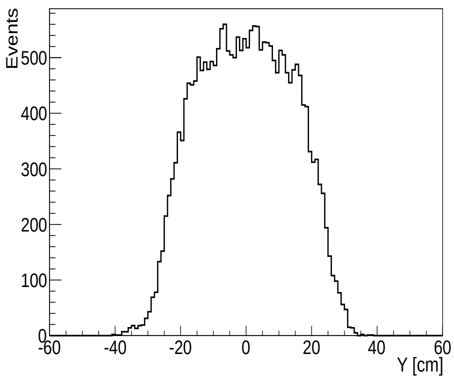


(b) Y position for fission fragments in the second MWPC.

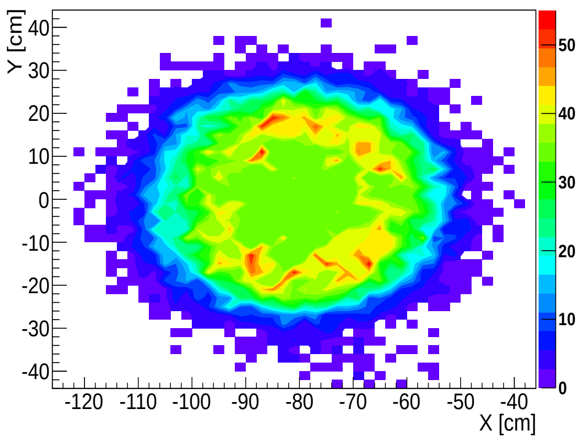


(c) Y vs. X position for fission fragments in the second MWPC.

***Figure 4.1:*** *Position for fission fragments in the second MWPC, collision* $^{238}U$+$^{238}U$.

We also simulated 12000 fission events for the reaction $^{208}$Pb+p with the INCL+ABLA code. The results of the propagation are shown in figure 4.2. One can see that the dispersion is 80 cm in X direction (see figure 4.2(a)) and 70 cm in Y direction (see figure 4.2(b)). Again we lose some fission fragments because our detector (MWPC) is 90×60 cm$^2$, being the corresponding efficiency 90 %. These calculations have been done with the detectors in the position X=-85 cm, Z= 695 cm and rotated 7°.

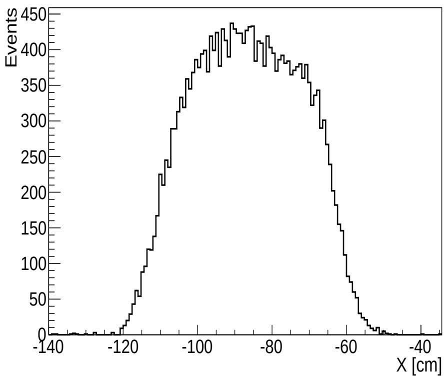


(a) X position for fission fragments in the second MWPC.

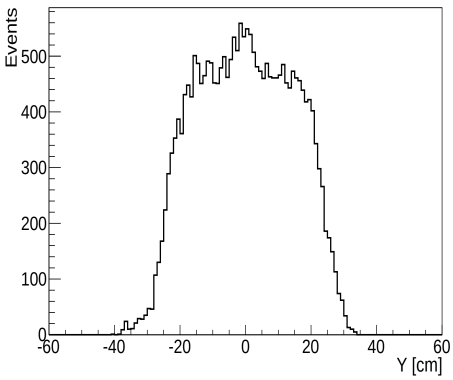


(b) Y position for fission fragments in the second MWPC.

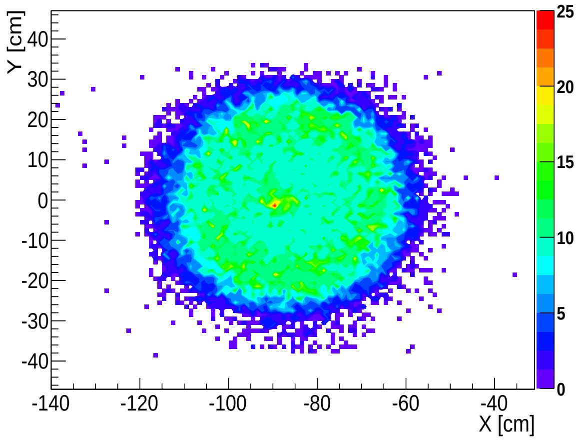


(c) Y vs. X position for fission fragments in the second MWPC.

***Figure 4.2:*** *Position for fission fragments in the second MWPC, collision* $^{208}Pb{+}p$.

### 4.1.3 Detection efficiency of light-charged particles

In addition, in the case of the reaction $^{208}$Pb+p we are interested in measuring the light-charged particles that are emitted in coincidence with the fission fragments. In order to provide a solution for the detection of light-charged particles we have investigated the range in polar angle covered by these particles in laboratory system as obtained from the reaction models. In figures 4.3 and 4.4 we show the polar angle ($\theta$) distribution in the laboratory for all light-charged particles produced in this reaction at 500 A MeV and 1 A GeV, respectively. In figure 4.3 we can see that the polar angles that corresponds to the maximum emission of cascade and evaporation protons is 160 and 120 mrad, respectively. This result indicates that the measurement of these protons after the ALADIN dipole is impossible because the aperture of ALADIN dipole is 60 mrad (y direction) and 338 mrad (x direction), similar results are obtained at 1 A GeV. For this reason we decided to put our tof-wall (see figure 2.9(a)) before ALADIN dipole between the vacuum pipe and the Twin MUSIC. The optimum position was determined by the simulation, to be 140 cm from the target. We will remove the two central vertical and horizontal paddles in this detector in order to leave an space

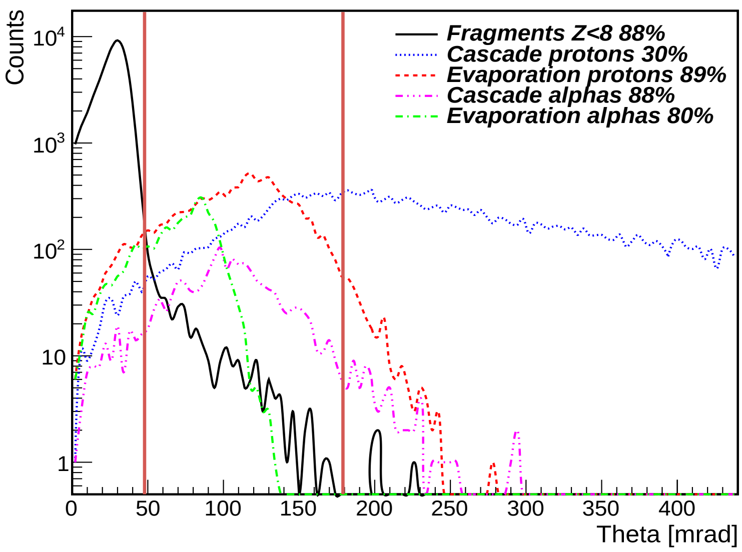


***Figure 4.3:*** *Polar angle distribution of light-charged particles emitted in coincidence with fission fragments in the reaction $^{208}$Pb+p at 500 A MeV. The two vertical lines delimit the geometrical acceptance of the Tof-wall we propose to use for the detection of light-charged particles.*

of 12×12 cm$^2$ for the transmission of fission fragments. These results yield a geometrical efficiency at 500 A MeV of 88 % for the detection of fragments with Z < 8, 30 % for the cascade protons, 89 % for the evaporation protons, 88 % for the cascade alphas and 80 % for the evaporation alphas. At 1 A GeV the results are 66 % for the fragments with Z < 8, 51 % for the cascade protons, 83 % for the evaporation protons, 85 % for the cascade alphas and 59 % for the evaporation alphas. The probability of having two particles on the same paddle was also calculated and it is about 4%.

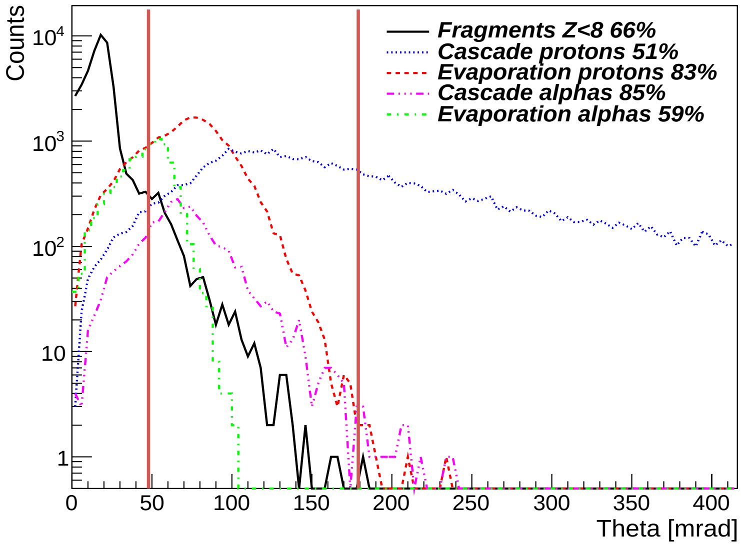


***Figure 4.4:*** *Same as figure 4.3 but for the reaction $^{208}$Pb+p at 1 A GeV.*

The results of the simulated angular distributions for all light-charged particles and ions up to Z = 8 are also shown in figures 4.3 (500 A MeV) and 4.4 (1 A GeV).

R3BRoot also allows to simulate the light-charged particles ToF-wall response, which help us to investigate if we can separate light-charged particles (protons, alphas, Li...). In figure 4.5 we show the energy loss in ToF-wall vs. time-of-flight which clearly shows a separation between light-charged particles where we have assumed a density of 1 g/cm$^3$ for the paddels.

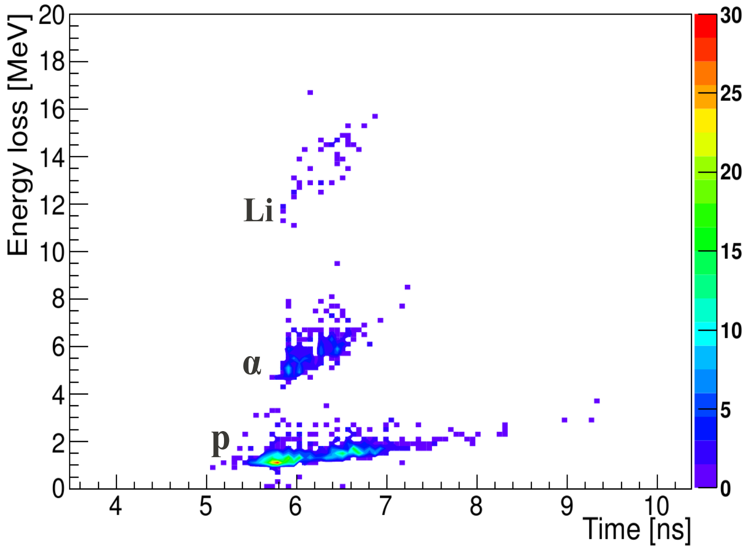


***Figure 4.5:*** *Energy loss vs. time-of-flight for light-charged particles on the tof-wall. We have simulated this figure with INCL+ABLA code.*

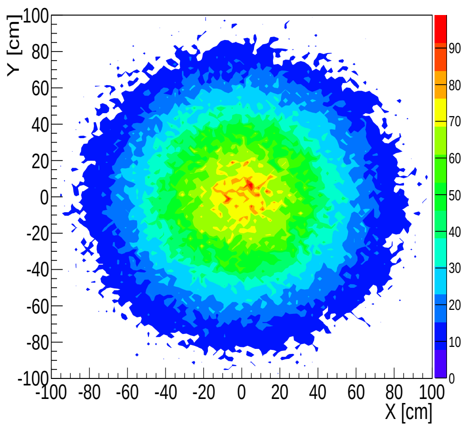


(a) Without matter.

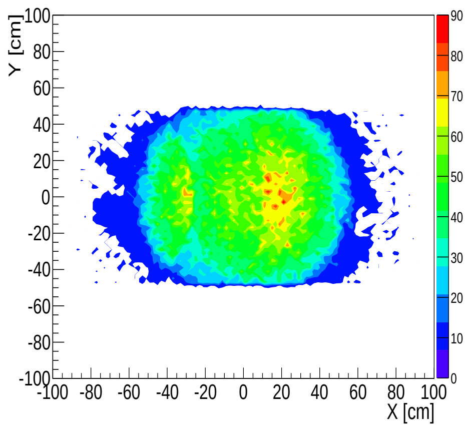


(b) With detectors, beam pipes and Aladin dipole.

***Figure 4.6:*** *Distribution of neutrons in LAND for collision $^{238}U$+$^{238}U$ at 500 A MeV. The geometrical efficiency is 88 % and the efficiency with detectors, beam pipes and Aladin dipole is 58 %.*

### 4.1.4 Detection efficiency of neutrons

Another quantity that can be calculated with the simulation is the neutron-detection efficiency with the LAND detector (see figure 2.10). First we simulate the propagation of neutrons produced in the reaction without matter for $^{238}$U+$^{238}$U and $^{208}$Pb+p (see figures 4.6(a) and 4.7(a)), i.e., without detectors, beam pipes and the ALADIN dipole. In this case we get a geometrical efficiency of 88 % and 85 % for the collisions $^{238}$U+$^{238}$U and $^{208}$Pb+p, respectively. In a second case we simulate the propagation including matter (see figures 4.6(b) and 4.7(b)), i.e., with detectors, beam pipes and the ALADIN dipole, and the efficiency reduces to 58 % and 53 % for the collisions $^{238}$U+$^{238}$U and $^{208}$Pb+p, respectively.

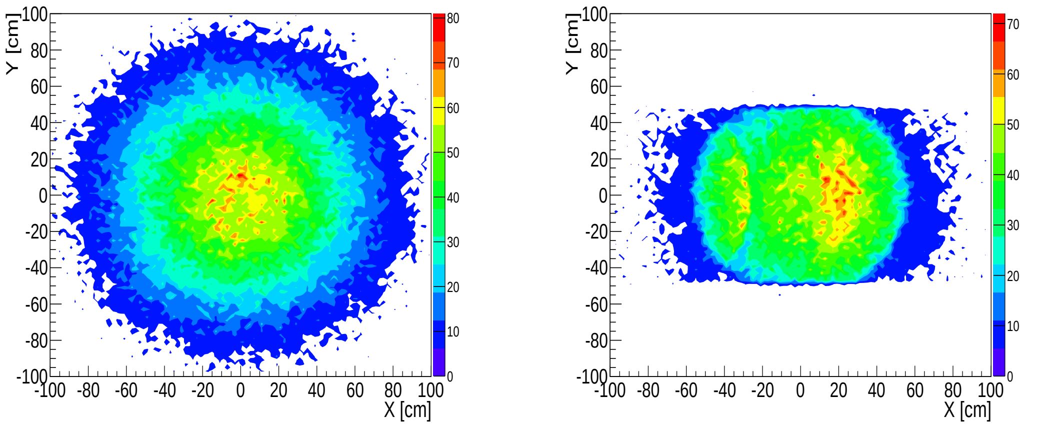


(a) Without matter.

(b) With detectors, beam pipes and Aladin dipole.

***Figure 4.7:*** *Distribution of neutrons in LAND for collision $^{208}$Pb+p at 500 A MeV. The geometrical efficiency is 85 % and the efficiency with detectors, beam pipes and Aladin dipole is 53 %.*

In figure 4.8, we represent the neutron multiplicity for cascade and evaporation neutrons produced by $^{238}$U+$^{238}$U collision. As can be seen, the mean number of neutrons is 20 (cascade plus evaporation), this means that we will measure 11 neutrons for each fission event. Figure 4.9 shows the neutron multiplicity for cascade and evaporation neutrons produced by $^{208}$Pb+p collision. In this case, the mean number of neutrons is 18 (cascade plus evaporation), this means that we will measure 9 neutrons for each fission event.

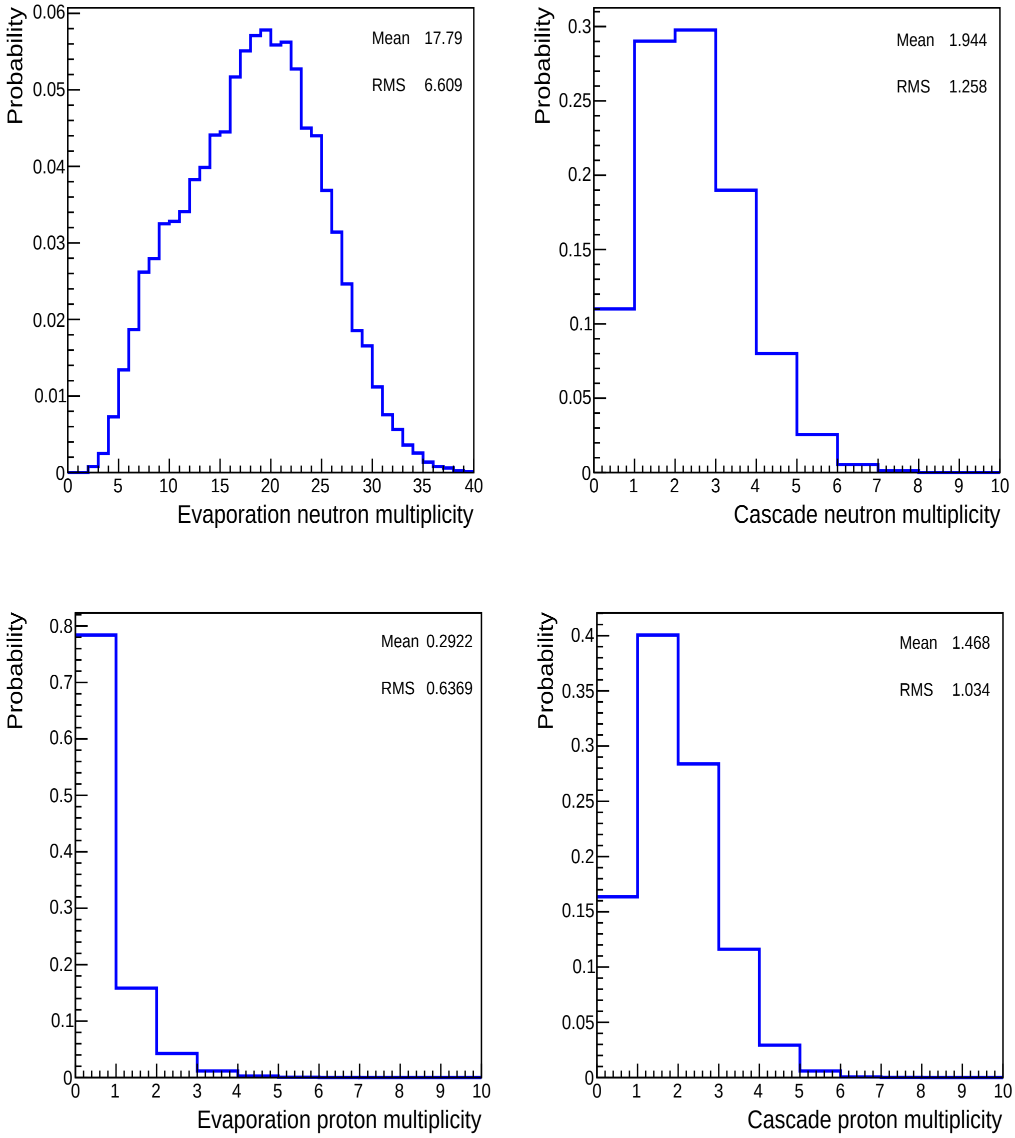


***Figure 4.8:*** *Multiplicity for protons and neutrons in* $^{238}U$+$^{238}U$ *collision at 500 A MeV.*

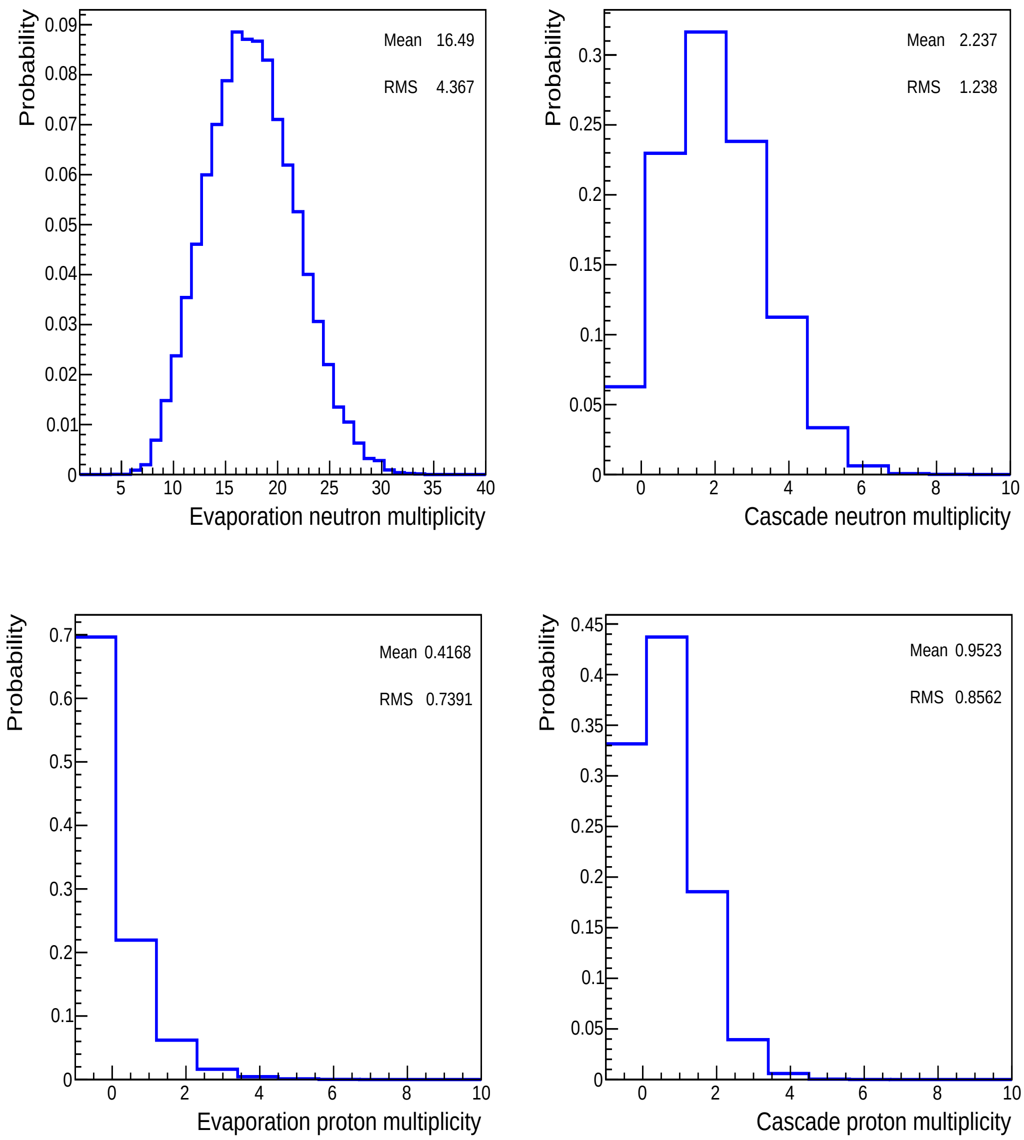


***Figure 4.9:*** *Multiplicity for protons and neutrons in $^{208}Pb+p$ collision at 500 A MeV.*

## 4.2 Reconstruction of the mass number

In principle, the trajectory of a fragment along our experimental steup will depend on the point of interaction, its magnetic rigidity and the entry and exit angles in the dipole. Our reconstruction consists of determining the magnetic rigidity and the mass for the fission fragments associated to our observables, which will be the positions on the detector (Twin MUSIC and MWPCs) and the time-of-flight (ToF-wall). The positions on the Twin MUSIC and the MWPCs allow to reconstruct the magnetic rigidity and the time-of-flight allows to reconstruct the mass number.
Previous simulation work performed in the framework of Geant3 [16] taught us that the final momentum resolution varies for different reconstruction methods. In that work, the method proposed to reconstruct the momentum used a grid of trajectories inside the dipole and now we have extended this method to reconstruct the mass. The new reconstruction method comprehends the following points:

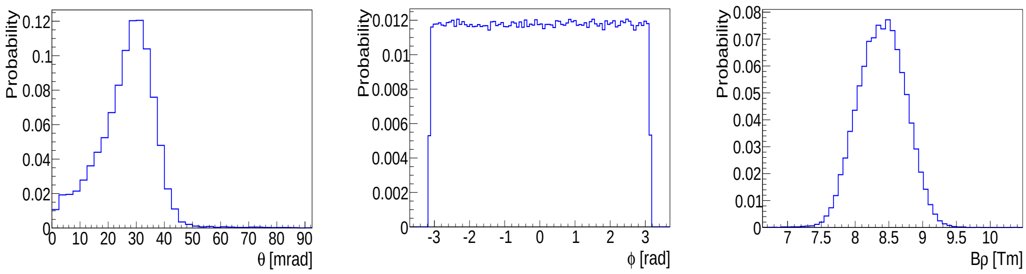


(a) $\theta$ distribution. (b) $\phi$ distribution. (c) B$\rho$ distribution.

***Figure 4.10:*** *$\theta$, $\phi$ and B$\rho$ theoretical distributions.*

- We create with the simulation program a 3D grid of reference trajectories (where we consider the ideal detectors) with defined values of B$\rho$, $\theta$ and $\phi$ and we register the corresponding positions at the three tracking detectors. The range in B$\rho$, $\theta$ and $\phi$ is obtained from simulations of the corresponding reactions using the INCL+ABLA code[2], as shown in the figures 4.10(a), 4.10(b) and 4.10(c). Then we simulate with $^{119}Sn$ the trajectories of the grid convering the range determined from the previous simulations and with a step in B$\rho$, $\theta$ and $\phi$ as indicated in table 4.1.
- We simulate fission events with the INCL+ABLA code, which will represent the real data or real trajectories.

[2]INCL+ABLA and ABRABLA codes give the same values for these variables.

| Variable | Init | Final | Step |
|---|---|---|---|
| $\theta$ [mrad] | 0 | 50 | 2.5 |
| $\phi$ $[rad]$ | -3.14 | 3.14 | 0.04 |
| B$\rho$ [Tm] | 7.3 | 9.7 | 0.025 |

***Table 4.1:*** *Parameters defining the reference grid of trajectories in the setup.*

- We reconstruct our real trajectories interpolating within the reference grid. For this we use a search algorithm to localise the closest trajectories in the reference grid using as parameter a maximum distance between the real trajectory and the trajectories of the grid, as

$$d_{max} > \sqrt{\sum_i ((X_{i,real} - X_{i,grid})^2 + (Y_{i,real} - Y_{i,grid})^2)} \tag{4.6}$$

where $(X_{i,real}, Y_{i,real})$ are the real positions and $(X_{i,grid}, Y_{i,grid})$ are the grid positions in the detector i. In our case we define $d_{max} = 5$ mm, this is a compromise between time of calculation and trajectories needed to have resolution enough.

- The trajectories found within d$_{max}$ are then fited using the class TMinuit of Root, this allowed us to reconstruct the magnetic rigidity and the trajectory length, for this we do two fits

$$B\rho = a_0 + a_1 X_{TM} + a_2 X_{MWPC1} + a_3 X_{MWPC2} \tag{4.7}$$

$$l = b_0 + b_1 X_{TM} + b_2 X_{MWPC1} + b_3 X_{MWPC2} \tag{4.8}$$

where $X_{TM}$, $X_{MWPC1}$ and $X_{MWPC2}$ are the positions in X direction found in the grid of trajectories for the detectors Twin MUSIC, first MWPC and second MWPC respectively. These fits allows us to know the coeficients $a_i$ and $b_i$. Now we only need to put the real position of the detectors in the equations 4.7 and 4.8 to get B$\rho$ and $l$ respectively.

- Finally we calculate the mass using the magnetic rigidity (B$\rho$) and the length ($l$), according to

$$A = \frac{0.299 Z B\rho}{0.931 \beta\gamma} \tag{4.9}$$

where $\beta = l$/t (t is the real time-of-flight).

### 4.2.1 Results of the reconstruction

First we check our reconstruction method. We simulate events of INCL+ ABLA in R3BRoot and we record the positions corresponding to the emitted fission fragments both in the Twin MUSIC, the MWPCs and the ToF-wall. Afterwards we use our reconstruction method to reconstruct these events and compare the results of the calculated value for reconstructed B$\rho$ with the nominal value given by the INCL+ABLA code each the fission fragment. This is shown in figure 4.11 where we can see that the B$\rho$ resolution is 0.5% (FWHM). This resolution allows us to reconstruct quite accurately the momentum of the fission fragments.

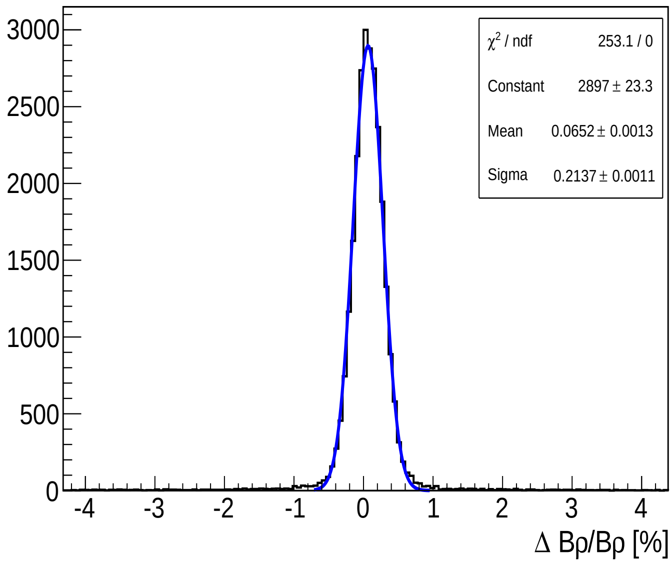


***Figure 4.11:*** *Resolving power for B$\rho$ obtained by using the reconstruction method with simulated fission fragments from INCL+ABLA code. The result shows a FWHM of 0.5% that would be precise enough for our purpose.*

Knowing that we need mass resolution better than 0.7 (FWHM) to separate two consecutive masses, we study how the mass resolution depends on our reconstruction method and the experimental setup (see figure 4.12). To do this, first we simulate with vacuum and with infinity resolution in the detectors (ideal detectors) and we obtain a FWHM of 0.10 (open circles), which represents the contribution of the reconstruction method to the mass resolution. Second we simulate with vacuum and with resolution in the position detectors (200 $\mu m$ in x and 2 mm in y) and we observe a FWHM around

0.15 (asterisk). Third we simulate with vacuum and with resolution in the ToF-wall detector (40 ps FWHM and we consider ideal position detectors) and we observe a FWHM of 0.3 (triangles) representing the contribution of the ToF to the mass resolution.

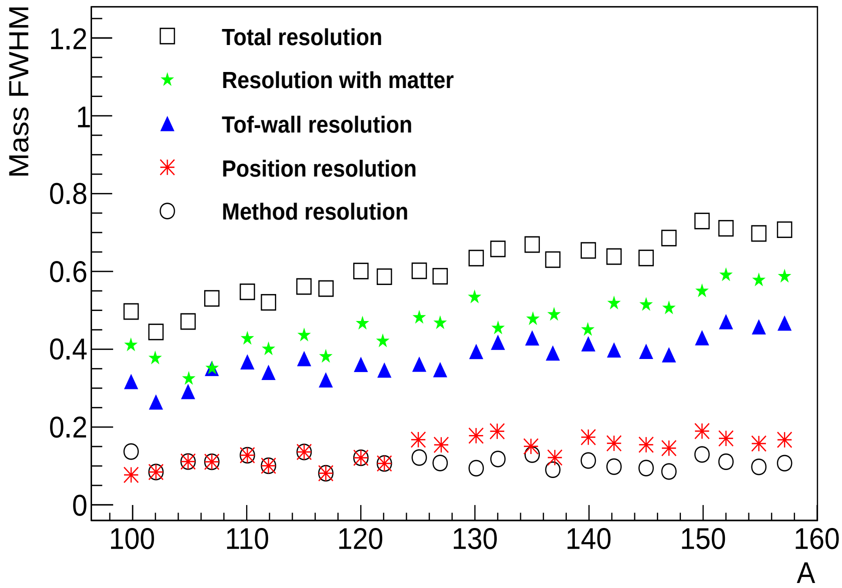


***Figure 4.12:*** *Mass FWHM vs. mass for fission fragments, we put some masses.*

Fourth we simulate the experimental setup with matter but infinity resolutions in the detectors (ideal detectors) and we observe a FWHM of 0.45 (stars). Finally we simulate the experimental setup and detector with realistic resolutions and we obtain a mass resolution (FWHM) below of 0.70 (open squares). The results of this figure show that our method is not limiting the mass resolution and that we are limited by the matter. Therefore we simulate different configurations of matter in the beam pipes (see figure 4.13 where Vacuum-He means that the pipes are: before the magnet - vacuum and after the magnet - helium). First we simulate with vacuum-He and we observe a mass resolution below of 0.70 (open squares). In the case of He-He, we also observe a mass resolution below of 0.70 (asterisk) but if we put Air the mass resolution is above of 0.70 (stars and open circles) which means that in these cases we cannot separate the mass, as shown in

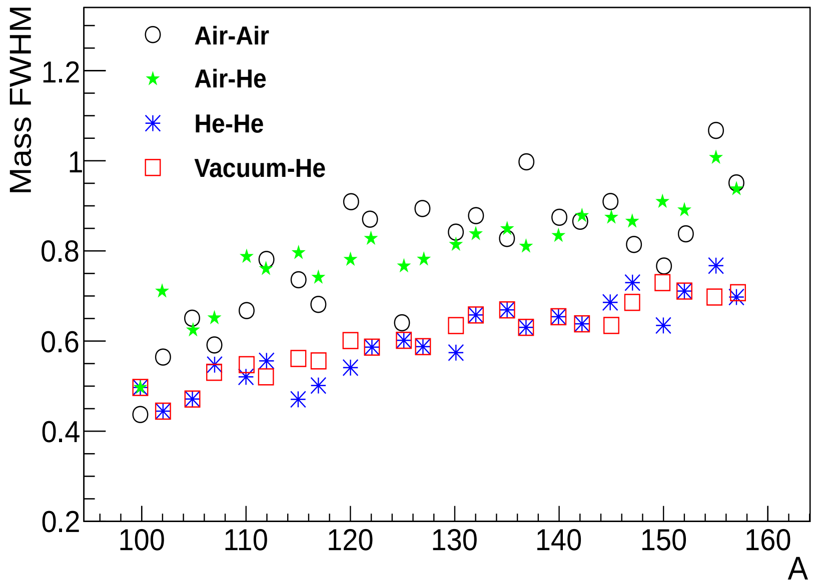


***Figure 4.13:*** *Mass FWHM vs. mass for different setup of beam pipes.*

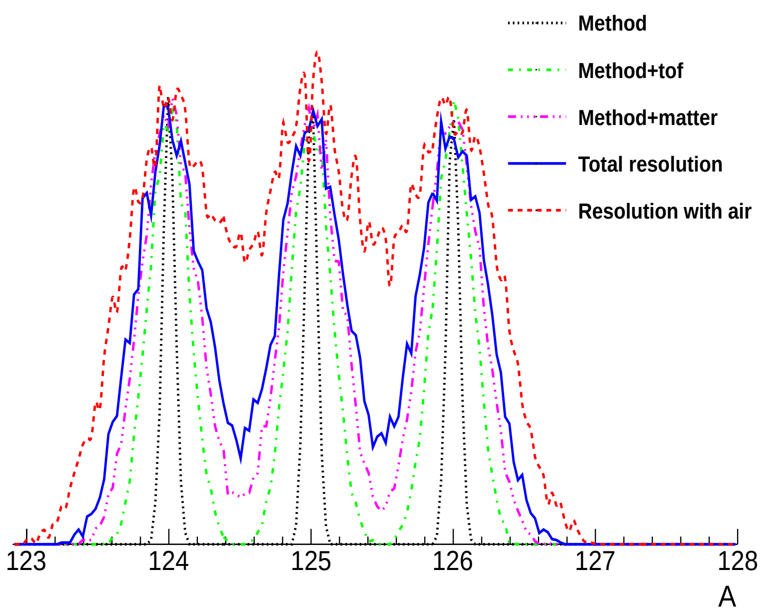


***Figure 4.14:*** *Representation of the mass FWHM for different cases of the figures 4.12 and 4.13.*

figure 4.14 where we display the distributions for three masses (124, 125 and 126) with different widths, where the black line represents the reconstruction method, the green line is our method plus ToF resolution, the pink line is our method plus angular straggling in matter, the blue line is our method plus resolution detectors plus angular straggling in matter and finally the red line is our resolution if we put air in the beam pipes. If we consider the results of the figures 4.12, 4.13 and 4.14 can conclude that we are limited by angular straggling in matter and that we need beam pipes with vacuum and helium or all helium to have mass resolution. In addition we can conclude that the resolution obtained with our experimental setup allows us to reconstruct with accuracy the mass of the fission fragments.

The mass resolution can also depend on the magnetic field, we check this effect changing the magnetic field in $\pm 2\%$, the results are shown in figure 4.15, where we can see that B$\rho$ resolution do not depend of the magnetic field while accurate value depends of it, this means that we need to know accurately the magnetic field to obtain trustable results in B$\rho$.

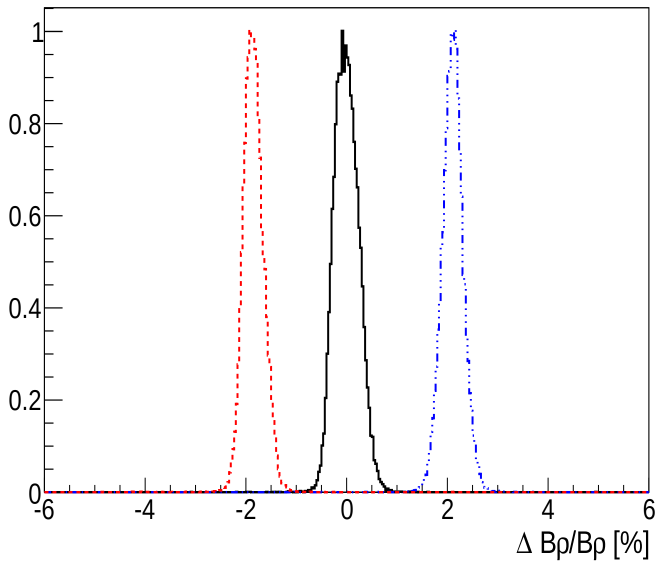


***Figure 4.15:*** *Resolving power for the $B\rho$ obtanined by using the reconstruction method with simulated fission fragments from INCL+ABLA code. The black solid line corresponds to the case of grid and data with a same magnetic field, the red dashed line corresponds to the same calculations but with a magnetic field decreased by 2% and the blue dot-dashed line corresponds with a magnetic field increased by 2%.*

In addition, we also checked the mass resolution when we change the magnetic field (see figure 4.16), for this we simulate different masses in our mass range for different cases: first we simulate with a magnetic field of 1.5 T (open squares), real magnetic field. Second we simulate with a same magnetic field but increased by 2% (open triangles), third we simulate with a same magnetic field but with a random variation of 2% (asterisk). These cases allow us to conclude that these magnetic field variations do not change the mass resolution. Finally we simulate with a magnetic field of 2.2 T (stars) and see that the mass resolution is better, as expected.

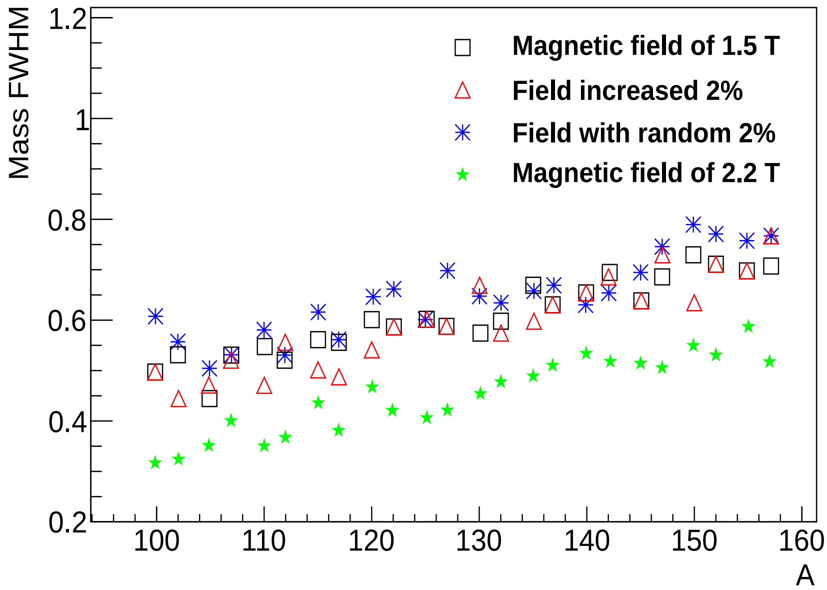


***Figure 4.16:*** *FWHM of the mass vs. mass for different magnetic fields, we put some masses.*

Finally we present the masses reconstructed for $^{238}$U+$^{238}$U and $^{208}$Pb+p collisions in figures 4.17, 4.18 and 4.19. In these reconstructions we use the positions on the Twin MUSIC, the MWPCs and the ToF-wall, in figure 4.17 we show the reconstruction of $\theta$, $\phi$ and B$\rho$ which show a accurate value. We see two holes in the $\phi$ distribution, at -1.57 and 1.57 rad which coincide with the anode position of the Twin MUSIC. In addition, in figures 4.18 and 4.19 we show the reconstruction of the fission fragments in the $^{238}$U+$^{238}$U and $^{208}$Pb+p collisions, respectively.

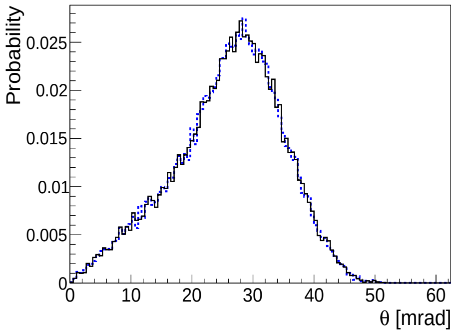


(a) $\theta$ distribution for $^{238}$U+$^{238}$U.

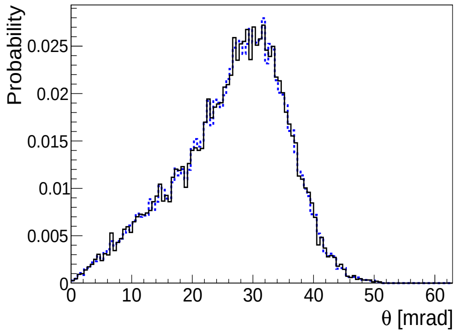


(b) $\theta$ distribution for $^{208}$Pb+p.

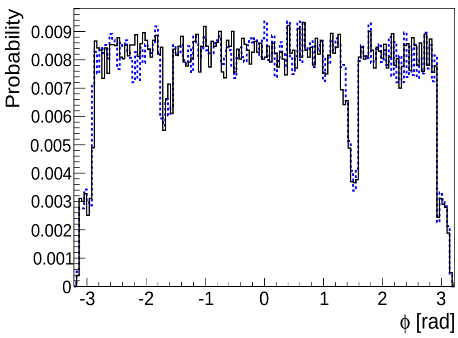


(c) $\phi$ distribution for $^{238}$U+$^{238}$U.

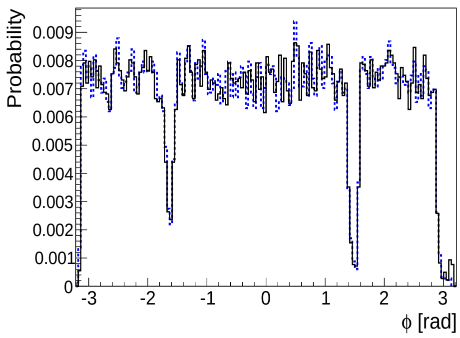


(d) $\phi$ distribution for $^{208}$Pb+p.

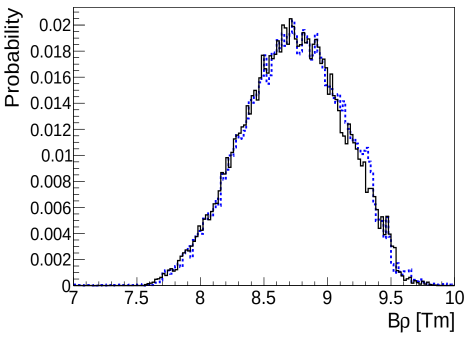


(e) B$\rho$ distribution for $^{238}$U+$^{238}$U.

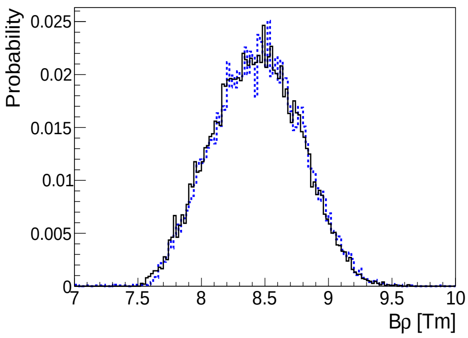


(f) B$\rho$ distribution for $^{208}$Pb+p.

***Figure 4.17:*** *$\theta$, $\phi$ and B$\rho$ reconstructed distributions for $^{238}U$+$^{238}U$ and $^{208}Pb$+p collisions coming from INCL+ABLA code. The black solid lines are the distributions obtained by INCL+ABLA code and blue dashed lines are the distributions obtained with the reconstruction method.*

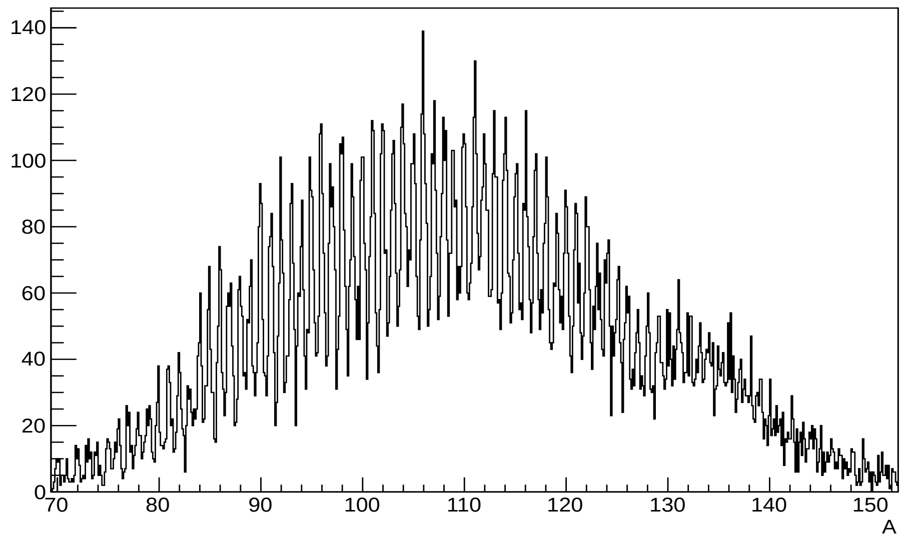


***Figure 4.18:*** *Masses reconstructed with our reconstruction method for* $^{238}U$+$^{238}U$ *collision.*

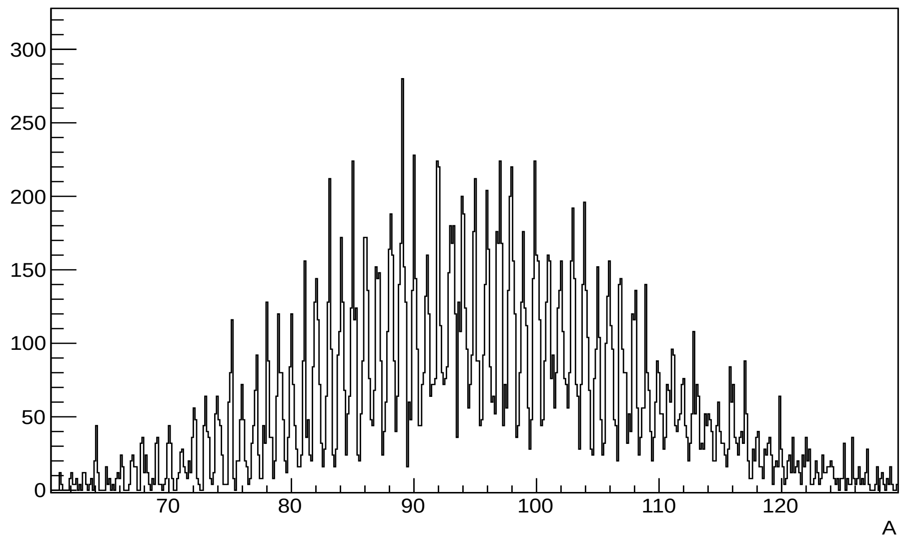


***Figure 4.19:*** *Masses reconstructed with our reconstruction method for* $^{208}Pb$+$p$ *collision.*

# Conclusions

In this work we have described the simulation of the SOFIA experiment, which has been made in GEANT4 with the R3BRoot interface.

The simulation provides the whole description of the different detectors as well as the physical processes that will take place during the experiment, which have been simulated with the ABRABLA and the INCL+ABLA codes. We have applied the simulation to the study of the electromagnetic fission in $^{238}$U and nuclear reactions in $^{208}$Pb at 500 A MeV.

The accuracy of the simulation for energy loss calculations has been tested and compared with real data getting a precision about 3%. In addition we have compared the energy and the angular straggling calculations in Geant4 with the results of AMADEUS code, which get a same results.

We have calculated the position of the all detectors for a magnetic field value of 1.4-1.5 T (nominal current 2000 A), which provides a geometrical efficiency of 98% for the fission fragments. We also have determined the optimum position of the light-charged particles ToF-wall which is 140 cm from the $H_2$ target.

We have implemented a tracking algorithm to reconstruct the momentum and the mass of the fission fragments which allows us to study the fission mechanism.

We conclude that this method can be easily used in the analysis of SOFIA experiment with momentum resolutions of about 0.5% (FWHM) and mass resolutions below of 0.7 (FWHM), but taking into account that the precise measurement of the magnetic field and detector positions is crucial for getting realistic and right results and that also need a vacuum pipe before magnet and a He pipe after magnet to achieve mass resolution.

# Appendix A

### GEANT4 Physics Libraries used for the simulations

• G4EmHadronBuilder

- G4hIonisation
- G4ionIonisation
- G4hMultipleScattering
- G4MultipleScattering

• G4EmMuonBuilder

- G4MuIonisation
- G4MuBremsstrahlung
- G4MuPairProduction
- G4MuMultipleScattering

• G4PenelopeQEDBuilder

- G4PenelopeCompton
- G4PenelopeGammaConversion
- G4PenelopePhotoElectric
- G4PenelopeRayleigh
- G4eMultipleScattering
- G4PenelopeIonisation
- G4PenelopeBremsstrahlung
- G4PenelopeAnnihilation

• G4LowEnergyQEDBuilder

- G4LowEnergyCompton
- G4LowEnergyGammaConversion

- G4LowEnergyPhotoElectric
- G4LowEnergyRayleigh
- G4PhotoElectricEffect
- G4LivermorePhotoElectricModel
- G4ComptonScattering
- G4LivermoreComptonModel
- G4GammaConversion
- G4LivermoreGammaConversionModel
- G4RayleighScattering
- G4LivermoreRayleighModel
- G4eMultipleScattering
- G4UniversalFluctuation
- G4eIonisation
- G4LivermoreIonisationModel
- G4eBremsstrahlung
- G4LivermoreBremsstrahlungModel
- G4eplusAnnihilation
- G4PenelopeAnnihilationModel

• R3BDecaysBuilder

- G4Decay

• EmhadronElasticBuilder

- G4HadronElasticProcess
- G4LElastic

• EmBinaryCascadeBuilder

- G4BinaryCascade
- G4ProtonInelasticProcess
- G4NeutronInelasticProcess
- G4HadronFissionProcess
- G4HadronCaptureProcess
- G4LFission
- G4LCapture

• EmIonBinaryCascadeBuilder

- G4LDeuteronInelastic

- G4BinaryLightIonreaction
- G4TipathiCrossSection
- G4IonShenCrossSection
- G4DeuteronInelasticProcess
- G4LEDeuteronInelastic
- G4LETritonInelastic
- G4LEAlphaInelastic
- G4HadronInelasticProcess
- G4BinaryLightIonReaction

• EmGammaNucleusBuilder

- G4PhotoNuclearProcess
- G4TheoFSGenerator
- G4GammanuclearReaction

# Appendix B

**Energy loss tables for different materials**

| E(MeV/A) | Proj. | Exp. data | Amadeus | Geant4 |
|---|---|---|---|---|
| 46 | $^{58}$Ni* | 8.12 | 7.85 | 8.19 |
| 92 | $^{58}$Ni* | 5.01 | 4.57 | 4.86 |
| 115.3 | $^{197}$Au† | 30.34 | 31.95 | 31.71 |
| 130.7 | $^{208}$Pb† | 30.35 | 31.36 | 31.27 |
| 201.8 | $^{208}$Pb† | 23.79 | 24.22 | 24.04 |
| 257.7 | $^{197}$Au† | 19.54 | 19.89 | 19.58 |
| 261 | $^{58}$Ni* | 2.48 | 2.90 | 2.35 |
| 430 | $^{58}$Ni† | 1.904 | 1.914 | 1.970 |
| 525.1 | $^{209}$Bi† | 15.81 | 16.26 | 15.69 |
| 780 | $^{136}$Xe† | 5.861 | 5,888 | 5.974 |
| 900 | $^{234}$U† | 16.64 | 16.87 | 16.62 |

***Table 4.2:*** *Stopping powers for beryllium target (* 0.01 cm and † 0.1 cm thickness). The stopping powers are measured in MeV $mg^{-1}$ $cm^2$.*

| E(MeV/A) | Proj. | Exp. data | Amadeus | Geant4 |
|---|---|---|---|---|
| 110.9 | $^{197}$Au* | 25.56 | 27.06 | 25.15 |
| 163.3 | $^{209}$Bi* | 22.82 | 22.95 | 21.98 |
| 258.8 | $^{209}$Bi* | 18.38 | 18.36 | 17.68 |
| 263.4 | $^{197}$Au† | 16.62 | 17.73 | 16.78 |
| 433 | $^{136}$Xe* | 6.22 | 6.19 | 6.20 |
| 495.2 | $^{209}$Bi* | 14.36 | 14.18 | 13.80 |
| 780 | $^{136}$Xe† | 5.08 | 5.09 | 4.91 |
| 874.7 | $^{209}$Bi* | 12,17 | 11.90 | 12.33 |
| 900 | $^{238}$U* | 14,70 | 14.59 | 15.04 |

***Table 4.3:*** *Stopping powers for copper target (* 0.01 cm and † 0.1 cm thickness). The stopping powers are measured in MeV $mg^{-1}$ $cm^2$.*

| E(MeV/A) | Proj. | Exp. data | Amadeus | Geant4 |
|---|---|---|---|---|
| 117 | $^{197}$Au† | 29.56 | 31.64 | 29.85 |
| 120.4 | $^{208}$Pb† | 31.02 | 33.15 | 30.58 |
| 162.8 | $^{209}$Bi† | 27.03 | 27.49 | 26.91 |
| 202.6 | $^{208}$Pb† | 1.35 | 23.64 | 23.11 |
| 264 | $^{58}$Ni* | 2.41 | 2.32 | 2.42 |
| 433 | $^{136}$Xe* | 7.1 | 7.08 | 7.19 |
| 498.6 | $^{209}$Bi† | 16.42 | 16.27 | 15.52 |
| 690 | $^{18}$O† | 0.12 | 0.13 | 0.15 |
| 780 | $^{136}$Xe† | 5.81 | 5.80 | 5.79 |
| 866.7 | $^{209}$Bi* | 13.78 | 13.64 | 13.93 |
| 900 | $^{238}$U† | 16.74 | 16.73 | 16.27 |

***Table 4.4:*** *Stopping powers for aluminium target (* 0.01 cm and † 0.1 cm thickness). The stopping powers are measured in MeV $mg^{-1}$ $cm^2$.*

# Appendix C

**Layers of matter in the beamline for Pb at 560 A MeV**

| Material | Thickness | E/A [MeV] | Material | Thickness | E/A [MeV] |
|---|---|---|---|---|---|
| Iron Windows | 4.07 | 559.73 | Glass Al | 0.61 | 539.46 |
| Glass B | 2.11 | 559.57 | Glass Si | 19.88 | 537.95 |
| Glass O | 28.44 | 557.25 | Glass K | 0.18 | 537.94 |
| Glass Na | 1.49 | 557.14 | Kapton C | 5.2 | 537.51 |
| Glass Al | 0.61 | 557.10 | Kapton H | 0.2 | 537.48 |
| Glass Si | 19.88 | 555.61 | Kapton N | 0.55 | 537.43 |
| Glass K | 0.18 | 555.59 | Kapton O | 1.57 | 537.30 |
| Music C | 22.52 | 553.74 | TPC | 18.29 | 536.08 |
| Music F | 142.38 | 542.70 | Kapton C | 5.2 | 535.65 |
| Music C | 4.35 | 542.34 | Kapton H | 0.2 | 535.61 |
| Music H | 0.29 | 542.32 | Kapton N | 0.55 | 535.57 |
| Music O | 2.32 | 542.13 | Kapton O | 1.57 | 535.44 |
| Glass B | 2.11 | 541.96 | Scin. C | 283.19 | 511.71 |
| Glass O | 28.44 | 539.62 | Scin. H | 26.41 | 508.05 |
| Glass Na | 1.49 | 539.51 | | | |

***Table 4.5:*** *Layers of matter in the beamline (thickness in $mg/cm^2$).*

**Layers of matter in the beamline for U at 700 A MeV**

| Material | Thickness | E/A [MeV] | Material | Thickness | E/A [MeV] |
|---|---|---|---|---|---|
| Iron Windows | 4.07 | 699.724 | Glass Si | 19.88 | 674.801 |
| Kapton C | 5.20 | 699.286 | Glass K | 0.18 | 674.788 |
| Kapton H | 0.20 | 699.251 | Plas. 1 C | 0.52 | 674.744 |
| Kapton N | 0.55 | 699.205 | Plas. 1 H | 0.0028 | 674.743 |
| Kapton O | 1.57 | 699.073 | Plas. 2 C | 0.52 | 674.699 |
| TPC 1 | 18.29 | 697.831 | Plas. 2 H | 0.0028 | 674.698 |
| Kapton C | 5.20 | 697.393 | Kapton C | 5.20 | 674.256 |
| Kapton H | 0.20 | 697.350 | Kapton H | 0.20 | 674.220 |
| Kapton N | 0.55 | 697.311 | Kapton N | 0.55 | 674.174 |
| Kapton O | 1.57 | 697.180 | Kapton O | 1.57 | 674.041 |
| Glass B | 2.11 | 697.013 | TPC 2 | 18.29 | 672.785 |
| Glass O | 28.44 | 694.627 | Kapton C | 5.20 | 672.342 |
| Glass Na | 1.49 | 694.514 | Kapton H | 0.20 | 672.306 |
| Glass Al | 0.61 | 694.468 | Kapton N | 0.55 | 672.260 |
| Glass Si | 19.88 | 692.931 | Kapton O | 1.57 | 672.126 |
| Glass K | 0.18 | 692.918 | Glass B | 2.11 | 671.950 |
| Music C | 22.52 | 691.077 | Glass O | 28.44 | 669.545 |
| Music F | 142.38 | 679.674 | Glass Na | 1.49 | 669.430 |
| Music C | 4.35 | 679.304 | Glass Al | 0.61 | 669.384 |
| Music H | 0.29 | 679.280 | Glass Si | 19.88 | 667.830 |
| Music O | 2.32 | 679.084 | Glass K | 0.18 | 667.817 |
| Glass B | 2.11 | 678.916 | Music C | 22.52 | 665.894 |
| Glass O | 28.44 | 676.510 | Music F | 142.38 | 654.418 |
| Glass Na | 1.49 | 676.396 | Music C | 4.35 | 654.044 |
| Glass Al | 0.61 | 676.350 | Music H | 0.29 | 654.019 |

***Table 4.6:*** *Layers of matter in the beamline (thickness in mg/cm$^2$).*

| Material | Thickness | E/A [MeV] |
|---|---|---|
| Music O | 2.32 | 653.821 |
| Glass B | 2.11 | 653.650 |
| Glass O | 28.44 | 651.216 |
| Glass Na | 1.49 | 651.101 |
| Glass Al | 0.61 | 651.054 |
| Glass Si | 19.88 | 649.488 |
| Glass K | 0.18 | 649.474 |
| Scin. C | 283.19 | 624.935 |
| Scin. H | 26.41 | 620.142 |

***Table 4.7:*** *Layers of matter in the beamline (thickness in mg/cm$^2$).*

# Bibliography


[1] N. Bohr, J. A. Wheeler. The mechanism of nuclear fission. *Phys. Rev.*, 56:426, 1939.

[2] K.-H. Schmidt, J. Benlliure and A.R. Junghans. Fission of nuclei far from stability. *Nucl. Phys. A*, 693:169, 2001.

[3] A.N. Andreyev et al. New type of asymmetric fission in proton-rich nuclei. *Phys. Rev. Lett.*, 105:252502, 2010.

[4] http://www.gsi.de.

[5] http://www.r3broot.gsi.de.

[6] http://www.fairroot.gsi.de.

[7] http://www.geant4.cern.ch.

[8] J.-J. Gaimard, K.-H. Schmidt. A reexamination of the abrasion-ablation model for the description of the nuclear fragmentation reaction. *Nucl. Phys. A*, 531:709, 1991.

[9] A. Boudard, J. Cugnon, S. Leray, C. Volant. Intranuclear cascade model for a comprehesive description of spallation reaction data. *Phys. Rev. C*, 66:615, 2002.

[10] A. Kelic, M. V. Ricciardi, K-H Schmidt. Towards a complete description of the decay channels of a nuclear system from spontaneous fission to multifragmentation. arxiv:0906.4193.v1. 2009.

[11] C. Böckstiegel, S. Steinhäser, J. Benlliure, H. -G. Clerc, A. Grewe, A. Heinz, M. de Jong, A. R. Junghans, J. Müller and K-H. Schmidt. Total kinetic energies and nuclear-charge yields in the fission of relativistic $^{233}$U secondary projectiles. *Phys. Lett. B*, 398:259, 1997.

[12] B. D. Wilkins, E. P. Steinberg, R. R. Cashman. Scission-point model of nuclear fission based on deformed-shell effects. *Phys. Lett. C.*

[13] J. Benlliure, E. Casarejos, D. Cortina-Gil, E. Hanelt, M.F. Ordóñez, K.-H. Schmidt. A fast algorithm for precise energy-loss calculations of high-energetic heavy ions. *NIM A*, 2001.

[14] Saúl Beceiro Novo. *Implementation of a Geant4 simulation for the R3B setup (FAIR)(R3BSIM): application to* $^{27}P$ *Coulomb dissociation.* PhD thesis, USC, 2008.

[15] V. Highland. Some practical remarks on multiple scattering. *Nucl. Instrum. and Methods A*, 129:497, 1975.

[16] C. Rodríguez-Tajes: Diploma thesis. *Characterization of the ALADIN setup at GSI for Coulomb Dissociation experiments.* PhD thesis, USC, 2006.

# List of Figures


1.1 a) We observe shell effects where the fission happens with Z=54 when one expect that it happens with Z=50. b) Asymmetric observed in the fission of $^{180}$Hg where the most probable light and heavy masses are $A_L$= 80 and $A_H$= 100, which is not expected. . 9

2.1 The GSI (Darmstadt) experimental facilities. In this drawing we can observe the two acceleration stages, the UNILAC and SIS, and the experimental areas, in particular the Fragment Separator (FRS) and Cave C. . . . . . . . . . . . . . . . . . . . . . . . . . 12
2.2 B$\rho$ vs. $\theta$ for the fission fragments produced in the fission of $^{238}$U at 500 A MeV, we have used ABRABLA code to simulate this figure. 13
2.3 B$\rho$ vs. $\theta$ for the fission fragments produced in the fission of $^{208}$Pb at 500 A MeV, we have used INCL+ABLA code to simulate this figure. . . . . . . . . . . . . . . . . . . . . . . . . . . . . . . . 14
2.4 Experimental setup for the SOFIA experiment, we will use this setup for the $^{238}$U+$^{238}$U collision, in the case $^{208}$Pb+p we will change the active target by $H_2$ target and we will put a ToF-wall for light charged particles between vacuum pipe and Twin MUSIC. 15
2.5 $H_2$ target. . . . . . . . . . . . . . . . . . . . . . . . . . . . . 16
2.6 Active target. . . . . . . . . . . . . . . . . . . . . . . . . . . . 17
2.7 Twin MUSIC. . . . . . . . . . . . . . . . . . . . . . . . . . . . 17
2.8 MWPC. . . . . . . . . . . . . . . . . . . . . . . . . . . . . . . 18
2.9 ToF-walls for SOFIA experiment. . . . . . . . . . . . . . . . . . . 19
2.10 LAND detector. . . . . . . . . . . . . . . . . . . . . . . . . . . 20
2.11 Dimensions of the gap in ALADIN dipole, all in mm. . . . . . . . 21
2.12 The Aladin magnetic field component in the $B_x$, $B_y$ and $B_z$ direction as a funtion the $r_x$, $r_y$ and $r_z$ direction (see figure 2.4). In the graph $B_y$ vs. $r_y$ we observe that the magnetic field is not symmetric but it is not important because the y dimension of Aladin is [-21, 21] cm. . . . . . . . . . . . . . . . . . . . . . . . . . . . . 22

2.13 B$\rho$ vs. $\theta$ for different ions at 500 A MeV and 700 A MeV. It shows the ALADIN acceptance. . . . . . . . . . . . . . . . . . . . . . . . . 23

3.1 $V_x^{cm}$ vs. $V_z^{cm}$ velocity for fission fragments produce in INCL+ABLA code for the collision p+$^{238}$U. . . . . . . . . . . . . . . . . . . . . . 26
3.2 $V_x^{cm}$ vs. $V_z^{cm}$ velocity for fission fragments produce in ABRABLA code for the collision $^{238}$U+$^{238}$U. . . . . . . . . . . . . . . . . . . . 26
3.3 Zpe as funtion of $\beta$ for different ions. . . . . . . . . . . . . . . . . . . 29
3.4 Beryllium target: Percentual difference between experimental and calculated stopping power with AMADEUS and the difference between experimental and calculated stopping power with Geant4 as a funtion of the incident ion energy per nucleon. . . . . . . . . . . 32
3.5 Cooper target: Percentual difference between experimental and calculated stopping power with AMADEUS and the difference between experimental and calculated stopping power with Geant4 as a funtion of the incident ion energy per nucleon. . . . . . . . . . . 32
3.6 Aluminium target: Percentual difference between experimental and calculated stopping power with AMADEUS and the difference between experimental and calculated stopping power with Geant4 as a funtion of the incident ion energy per nucleon. . . . . . . . . . . 33

4.1 Position for fission fragments in the second MWPC, collision $^{238}$U+$^{238}$U. 42
4.2 Position for fission fragments in the second MWPC, collision $^{208}$Pb+p. 43
4.3 Polar angle distribution of light-charged particles emitted in coincidence with fission fragments in the reaction $^{208}$Pb+p at 500 A MeV. The two vertical lines delimit the geometrical acceptance of the Tof-wall we propose to use for the detection of light-charged particles. . . . . . . . . . . . . . . . . . . . . . . . . . . . . . 44
4.4 Same as figure 4.3 but for the reaction $^{208}$Pb+p at 1 A GeV. . . . 45
4.5 Energy loss vs. time-of-flight for light-charged particles on the tof-wall. We have simulated this figure with INCL+ABLA code. . 46
4.6 Distribution of neutrons in LAND for collision $^{238}$U+$^{238}$U at 500 A MeV. The geometrical efficiency is 88 % and the efficiency with detectors, beam pipes and Aladin dipole is 58 %. . . . . . . . . . 46
4.7 Distribution of neutrons in LAND for collision $^{208}$Pb+p at 500 A MeV. The geometrical efficiency is 85 % and the efficiency with detectors, beam pipes and Aladin dipole is 53 %. . . . . . . . . . 47
4.8 Multiplicity for protons and neutrons in $^{238}$U+$^{238}$U collision at 500 A MeV. . . . . . . . . . . . . . . . . . . . . . . . . . . . . . . . . 48
4.9 Multiplicity for protons and neutrons in $^{208}$Pb+p collision at 500 A MeV. . . . . . . . . . . . . . . . . . . . . . . . . . . . . . . . . 49

4.10 $\theta$, $\phi$ and B$\rho$ theoretical distributions. . . . . . . . . . . . . . . . 50
4.11 Resolving power for B$\rho$ obtained by using the reconstruction method with simulated fission fragments from INCL+ABLA code. The result shows a FWHM of 0.5% that would be precise enough for our purpose. . . . . . . . . . . . . . . . . . . . . . . . . . . . . . 52
4.12 Mass FWHM vs. mass for fission fragments, we put some masses. . 53
4.13 Mass FWHM vs. mass for different setup of beam pipes. . . . . . 54
4.14 Representation of the mass FWHM for different cases of the figures 4.12 and 4.13. . . . . . . . . . . . . . . . . . . . . . . . . . . 54
4.15 Resolving power for the B$\rho$ obtanined by using the reconstruction method with simulated fission fragments from INCL+ABLA code. The black solid line corresponds to the case of grid and data with a same magnetic field, the red dashed line corresponds to the same calculations but with a magnetic field decreased by 2% and the blue dot-dashed line corresponds with a magnetic field increased by 2%. . . . . . . . . . . . . . . . . . . . . . . . . . . . . . 55
4.16 FWHM of the mass vs. mass for different magnetic fields, we put some masses. . . . . . . . . . . . . . . . . . . . . . . . . . . . 56
4.17 $\theta$, $\phi$ and B$\rho$ reconstructed distributions for $^{238}$U+$^{238}$U and $^{208}$Pb+p collisions coming from INCL+ABLA code. The black solid lines are the distributions obtained by INCL+ABLA code and blue dashed lines are the distributions obtained with the reconstruction method. . . . . . . . . . . . . . . . . . . . . . . . . . . 57
4.18 Masses reconstructed with our reconstruction method for $^{238}$U+$^{238}$U collision. . . . . . . . . . . . . . . . . . . . . . . . . . . . . 58
4.19 Masses reconstructed with our reconstruction method for $^{208}$Pb+p collision. . . . . . . . . . . . . . . . . . . . . . . . . . . . . 58